

Two-scale topology optimization for composite plates with in-plane periodicity

Shinnosuke Nishi¹, Kenjiro Terada^{2,*},, Junji Kato³, Shinji Nishiwaki⁴ and Kazuhiro Izui⁴

¹*Department of Civil and Environmental Engineering, Tohoku University, 468-1 Aza-Aoba, Aramaki, Aoba-ku Sendai, 980-0845, Japan*

²*International Research Institute of Disaster Science, Tohoku University, 468-1 Aza-Aoba, Aramaki, Aoba-ku, Sendai, 980-0845, Japan*

³*Department of Civil and Environmental Engineering, Tohoku University, 6-6-06 Aza-Aoba, Aramaki, Aoba-ku, Sendai, 980-8597, Japan*

⁴*Department of Mechanical Engineering and Science, Kyoto University, Kyotodaigaku-katsura CIII, Nishikyo-ku, Kyoto, 615-8540, Japan*

SUMMARY

This study proposes a two-scale topology optimization method for a microstructure (an in-plane unit cell) that maximizes the macroscopic mechanical performance of composite plates. The proposed method is based on the in-plane homogenization method for a composite plate model in which the macrostructure is modeled using thick plate theory and the microstructures are three-dimensional solids. Macroscopic plate characteristics such as homogenized plate stiffnesses and generalized thermal strains are evaluated through the application of numerical plate tests applied to an in-plane unit cell. To handle large rotations of the composite plates, we employ a co-rotational formulation that facilitates working with the two-scale plate model formulated within a small strain framework. Two types of objective functions are tested in the presented optimization problems: one minimizes the macroscopic end compliance to maximize the macroscopic plate stiffness, whereas the other maximizes components of a macroscopic nodal displacement vector. Analytical sensitivities are derived based on in-plane homogenization formulae so that a gradient-based method can be employed to update the topology of in-plane unit cells. Several numerical examples are presented to demonstrate the proposed method's capability related to the design of optimal in-plane unit cells of composite plates. Copyright © 2017 John Wiley & Sons, Ltd.

Received 6 September 2016; Revised 2 March 2017; Accepted 3 March 2017

KEY WORDS: multiscale topology optimization; analytical sensitivities; composite plates; in-plane homogenization; co-rotational formulation

1. INTRODUCTION

Plates with heterogeneous local structures, generally called ‘composite plates’, are actively utilized in a variety of industrial fields such as the airplane, aerospace, and automobile industries. Most commonly, one or more types of local structures are arranged periodically in the in-plane directions, each of which can be termed an ‘in-plane unit cell’, as illustrated in Figure 1. Because the local structures determine overall structural characteristics such as bending and torsional stiffnesses, it is desirable to control their topologies is desirable, to enhance additional performances (e.g., to reduce weight and achieve a targeted flexibility). In this context, because Bendsøe and Kikuchi [1] and Suzuki and Kikuchi [2] first publicized a structural topology optimization method that incorporates a mathematical homogenization theory, it has become widely utilized to determine optimal material distributions

*Correspondence to: Kenjiro Terada, International Research Institute of Disaster Science, Tohoku University, 468-1, Aramaki, Aoba-ku, Sendai 980-0845, Japan.

†Email: tei@irides.tohoku.ac.jp

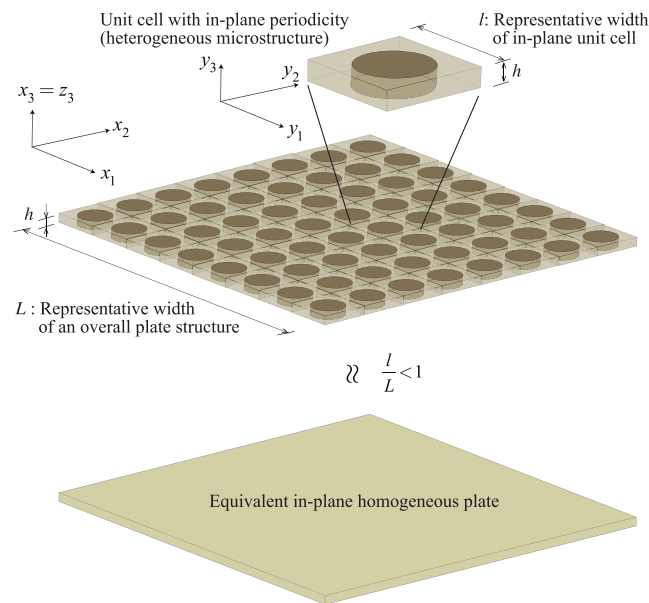


Figure 1. Concept of homogenization for composite plate with in-plane periodic microstructure.

in design regions. Comprehensive reviews of previously developed topology optimization methods can be found elsewhere; see, for example, References [3–6] and references therein.

In any event, most of the developments in topology optimization have addressed structures only on a single spatial scale. Although some articles are devoted to the topology optimization of microstructures, only a few attempts have so far been made to study topology optimization methods that account for the interaction between macrostructures and microstructures. Nevertheless, in recent years, there has been a growing interest in such ‘multiscale topology optimization’, which depends on solving the so-called two-scale boundary value problem (BVP) derived within the framework of homogenization theory [7]. For example, Rodrigues *et al.* [8] propose a hierarchical approach to simultaneously determine the topologies of both macrostructures and microstructures for linearly elastic materials. A similar approach proposed by Nakshatrala *et al.* [9] assumes the existence of hyperelastic materials in microstructures, assisted by the method of fully coupled nonlinear two-scale analyses [7]; see, for example, [10] for a more recent development. In these studies, each Gauss point or divided region of the macroscopic finite element (FE) model, whose topologies are intended to be optimized simultaneously, is associated with a single microstructure, and the topologies of all the microstructures are determined separately.

In contrast, Huang *et al.* [11] present a multiscale optimization scheme for a single topology of periodic microstructures in the macrostructure, a so-called uniformly structured material, for the optimal design of cellular materials. Furthermore, Kato *et al.* [12] propose a multiscale topology optimization based on a decoupling multiscale analysis method for nonlinear solids [13], in which microscale and macroscale nonlinear analyses are decoupled. This method depends on the method of numerical material testing to determine a single topology within a fixed macrostructural topology. A hierarchical approach is also taken by Vicente *et al.* [14] to determine a macrostructural topology that minimizes the eigenfrequencies of the macrostructure based on the optimization of a single microstructural topology. Additional recent progress in multi-scale topology optimization methods are presented in Yan *et al.* [15], Xia and Breitkopf [16, 17], Long *et al.* [18], and Da *et al.* [19].

Although there has been a great deal of research has been carried out to date concerning multiscale structural topology optimization, in which both microstructures and macrostructures are two-dimensional or three-dimensional (2D/3D) solids, no previous studies have presented a multiscale structural topology optimization method for composite plates with in-plane unit cells. The following facts are considered to be obstacles when following this path of research:

- The standard homogenization theory for 3D solids [20, 21] assumes that 3D heterogeneous microstructures are periodic, whereas composite plates have periodicity only in the in-plane directions (Figure 1);
- Whereas the representative length of the microstructures is assumed to be infinitesimally small compared with that of the macrostructure in standard homogenization theory, the thickness of an in-plane unit cell must be the same as that of a macroscopic plate. This implies that the limit cannot be taken as the volume of the unit cell approaches zero; and
- Whereas 3D solid models are employed when formulating the governing equations at both scales in standard homogenization theory, the overall mechanical behavior of composite plates must be described using thick plate theory, in which resultant stresses must be evaluated through 3D analyses of an in-plane unit cell.

In short, multiscale modeling for composite plates with in-plane periodicity has not been fully established. In particular, the second item set forth above conflicts with the mathematical theory of homogenization [20, 21] and has never been explored. Inevitably, previous research on the optimization for composite plates has been limited to 2D optimization of in-plane periodic local structures [22] and 3D size optimization of members of sandwich panels [23, 24]. In this context, Terada *et al.* [25] have recently proposed an innovative two-scale analysis method for composite plates by applying the idea of numerical material testing [13] to classical thick plate theory. In their method, thick plate theory is applied to macroscopic plates, whereas a 3D solid is employed for the in-plane unit cells. The microscopic analysis for in-plane unit cells uses numerical plates testing (NPT) to ‘measure’ the homogenized thick plate stiffnesses (in-plane tension/compression/shear, bending, and torsional stiffnesses, along with transverse-shear stiffnesses). In this study, we incorporate this new and original method of NPT to construct a method for two-scale topology optimization of composite plates, to determine optimum topologies of in-plane unit cells that maximize macroscopic mechanical performances. In addition, the method is extended to include thermal excitation because thermal deformations are easily introduced in the current NPT format. Through the NPT method, the proposed two-scale topology optimization method enables us to obtain optimal topologies of in-plane periodic 3D cross-sectional structures of composite plates.

While developing the method presented here, we also wanted to consider large translations and rotation of the composite plates so that the two-scale topology optimization could be applied to design and control the functionalities of composite plates for application in actuators and other flexible devices. When working with such large displacements, the assumption of linear kinematics is no longer valid. In the first decade of the 2000s, certain geometrical nonlinearities were incorporated into topology optimization formulations, for example, by Buhl *et al.* [26], Bruns and Tortorelli [27], Gea and Luo [28], Jung and Gea [29], and Cho and Jung [30]. In their reports, geometrically nonlinear problems are described using the total Lagrangian or updated Lagrangian formulations, to which finite strain is commonly introduced. However, these formulations appear to be intractable in a two-scale analysis method for composite plates [25], because the small strain framework is the premise for obtaining homogenized plate stiffnesses with NPT, and its extension to large deformations is far from trivial. To manage small strains and large translation/rotation simultaneously, we employ the so-called co-rotational (CR) formulation [31–33], in which the motion of each plate’s FE is decomposed into two types: one for rigid body motion and the other for elastic deformation under the assumption of infinitesimal strain. In this way, in-plane homogenization [25] can be applied for the elastic deformation, and some minor adjustments are made to follow the rigid body motion.

In Section 2, we summarize the in-plane homogenization method and present formulae for computing the homogenized plate stiffness matrix and the macroscopic thermal stress, thus reflecting the topologies of in-plane unit cells. The CR formulation is then introduced to address large displacements (translations and rotations) during the in-plane homogenization process. Section 3 is devoted to the formulation of the two-scale topology optimization method. In this study, to determine one or more topologies of in-plane unit cells, we focus on two specific objective functions, which respectively aim to maximize the overall stiffness and certain components of a nodal displacement vector.

In addition, the sensitivities of the employed objective functions and the homogenized plate stiffnesses are analytically derived, and the accuracy of these derivations is verified through comparison with results obtained by numerical differentiation. In Section 4, several numerical examples are presented to demonstrate the efficiency and capability of the proposed method for the design of locally repeated structures of composite plates. Section 5 concludes this study and raises issues that we hope to address in future work.

2. MULTISCALE MODELING OF COMPOSITE PLATES

2.1. In-plane homogenization method

In this section, we summarize the two-scale model for composite plates with in-plane periodicity, which was originally proposed in Reference [25]. The two-scale BVP given here is composed of a microscopic BVP for a 3D solid domain of an in-plane unit cell and a macroscopic BVP described according to standard thick plate theory. We also present a homogenized plate stiffness matrix for the macroscopic thick plate and a generalized thermal stress vector, which are intended to appropriately reflect the microscale topologies of in-plane unit cells.

As in Figure 2, which illustrates a cross-sectional diagram viewed along the x_2 -direction, the macroscopic displacement fields $u_i (i = 1 \sim 3)$ in thick plate theory are given by

$$\begin{cases} u_1(x_1, x_2; x_3) = \bar{u}_1(x_1, x_2) - x_3 \phi_1(x_1, x_2) \\ u_2(x_1, x_2; x_3) = \bar{u}_2(x_1, x_2) - x_3 \phi_2(x_1, x_2) \\ u_3(x_1, x_2) = \bar{u}_3(x_1, x_2) \end{cases} \quad (1)$$

where $u_a (a = 1, 2)$ is the in-plane displacements on the neutral plane and $\phi_a (a = 1, 2)$ indicates the rotation angles of the vertical sections with respect to the x_1 and x_2 axes, respectively. Additionally, $N_a, M_a, V_a (a = 1, 2)$ in Figure 2 respectively indicate the in-plane generalized (resultant) stresses, bending moments, and transverse resultant shear stresses for the cross section. Thus, the macroscopic strain can be computed as

$$\mathbf{E} = \begin{Bmatrix} E_{11} \\ E_{22} \\ E_{33} \\ 2E_{12} \\ 2E_{23} \\ 2E_{31} \end{Bmatrix} = \begin{Bmatrix} \frac{\partial \bar{u}_1}{\partial x_1} - x_3 \frac{\partial \phi_1}{\partial x_1} \\ \frac{\partial \bar{u}_2}{\partial x_2} - x_3 \frac{\partial \phi_2}{\partial x_2} \\ 0 \\ \frac{\partial \bar{u}_1}{\partial x_2} + \frac{\partial \bar{u}_2}{\partial x_1} - x_3 \left(\frac{\partial \phi_2}{\partial x_1} + \frac{\partial \phi_1}{\partial x_2} \right) \\ \frac{\partial \bar{u}_3}{\partial x_2} - \phi_2 \\ \frac{\partial \bar{u}_3}{\partial x_1} - \phi_1 \end{Bmatrix} = \begin{Bmatrix} \tilde{E}^1 + x_3 \tilde{E}^4 \\ \tilde{E}^2 + x_3 \tilde{E}^5 \\ 0 \\ \tilde{E}^3 + x_3 \tilde{E}^6 \\ \tilde{E}^7 \\ \tilde{E}^8 \end{Bmatrix} \quad (2)$$

Here, $\tilde{E}^I (I = 1 \sim 8)$ is the generalized macroscopic strains, defined as

$$\begin{aligned} \tilde{\mathbf{E}} &= \{ \tilde{E}^1 \ \tilde{E}^2 \ \tilde{E}^3 \ \tilde{E}^4 \ \tilde{E}^5 \ \tilde{E}^6 \ \tilde{E}^7 \ \tilde{E}^8 \}^T \\ &= \left\{ \frac{\partial \bar{u}_1}{\partial x_1} \ \frac{\partial \bar{u}_2}{\partial x_2} \ \frac{\partial \bar{u}_3}{\partial x_1} + \frac{\partial \bar{u}_1}{\partial x_2} \ - \frac{\partial \phi_1}{\partial x_1} \ - \frac{\partial \phi_2}{\partial x_2} \ - \left(\frac{\partial \phi_2}{\partial x_1} + \frac{\partial \phi_1}{\partial x_2} \right) \ \frac{\partial \bar{u}_3}{\partial x_2} \ - \phi_2 \ \frac{\partial \bar{u}_3}{\partial x_1} \ - \phi_1 \right\}^T \end{aligned} \quad (3)$$

whose deformation modes are depicted in Figure 3.

The microscopic strain ϵ is defined as the sum of the macroscopic strain and microscopic strain fluctuations, thus

$$\epsilon = \tilde{z} \tilde{\mathbf{E}} + \partial_y \mathbf{u}^*, \quad (4)$$

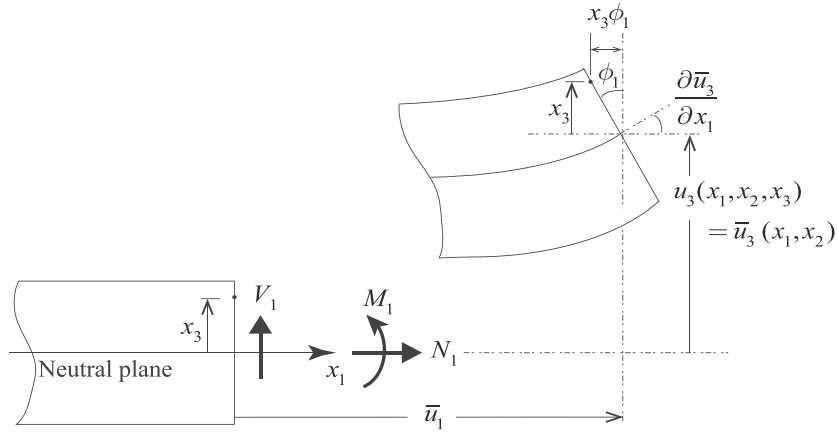


Figure 2. Displacement fields in thick plate theory.

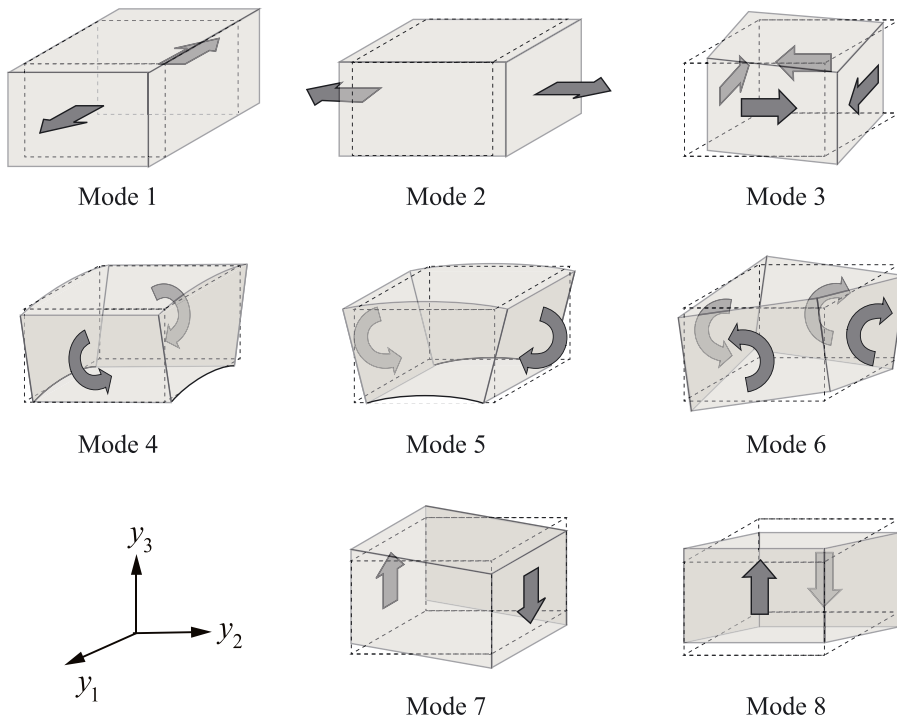


Figure 3. Deformation modes represented as generalize macroscopic strains.

where we have defined the following matrix expressions:

$$\tilde{z} = \begin{bmatrix} 1 & 0 & 0 & z_3 & 0 & 0 & 0 & 0 \\ 0 & 1 & 0 & 0 & z_3 & 0 & 0 & 0 \\ 0 & 0 & 0 & 0 & 0 & 0 & 0 & 0 \\ 0 & 0 & 1 & 0 & 0 & z_3 & 0 & 0 \\ 0 & 0 & 0 & 0 & 0 & -z_1/2 & 1 & 0 \\ 0 & 0 & 0 & 0 & 0 & -z_2/2 & 0 & 1 \end{bmatrix} \quad \text{and} \quad \partial_y \mathbf{u}^* = \begin{bmatrix} \frac{\partial}{\partial y_1} & 0 & 0 \\ 0 & \frac{\partial}{\partial y_2} & 0 \\ 0 & 0 & \frac{\partial}{\partial y_3} \\ \frac{\partial}{\partial y_2} & \frac{\partial}{\partial y_1} & 0 \\ 0 & \frac{\partial}{\partial y_3} & \frac{\partial}{\partial y_2} \\ \frac{\partial}{\partial y_3} & 0 & \frac{\partial}{\partial y_1} \end{bmatrix} \begin{Bmatrix} u_1^* \\ u_2^* \\ u_3^* \end{Bmatrix} \quad (5)$$

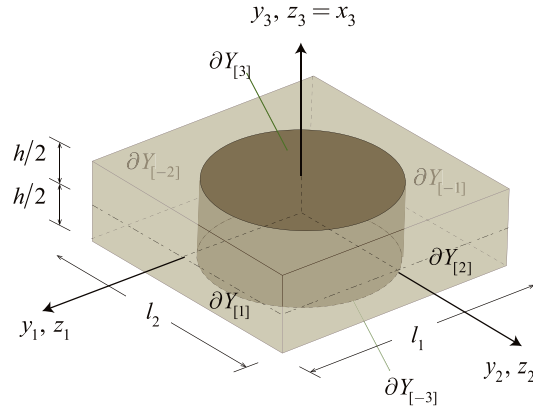


Figure 4. In-plane unit cell.

Here, two coordinate systems, y_i and z_i , are used in these equations. Whereas y_i is the microscale coordinate system used for the homogenization process, z_i are merely kinematic parameters used to represent the kinematics in the standard plate theory. Note that z_i is identified with the macroscale coordinate system used in formulating the macroscopic equations; see Figure 4. Moreover, matrix \tilde{z} transforms the generalized macroscopic strain into a microscopic strain whose components are independent of the microscale heterogeneities. Here, components $-z_1/2$ and $-z_2/2$ may appear undesirable but are required for consistency with the macroscopic torsional deformations; see [25] for a detailed explanation. Finally, $\partial_y \mathbf{u}^*(\mathbf{y})$ is the microscopic strain fluctuation excited by microscale heterogeneities, and \mathbf{u}^* is the corresponding displacement field that is intended to satisfy the in-plane periodic boundary conditions, or, equivalently, ‘in-plane Y-periodicity’.

Using the aforementioned expressions, we formulate the following set of governing equations for the microscopic BVP for an in-plane unit cell domain, $Y = l_1 l_2 l_3$:

$$\begin{cases} \partial_y^T \boldsymbol{\sigma} = 0 \\ \boldsymbol{\sigma} = \mathbf{C} (\boldsymbol{\varepsilon} - \boldsymbol{\varepsilon}^{\text{th}}) \\ \boldsymbol{\varepsilon} = \tilde{z} \tilde{\mathbf{E}} + \partial_y \mathbf{u}^* = \partial_y \mathbf{w} \\ \boldsymbol{\varepsilon}^{\text{th}} = \alpha \Delta T \boldsymbol{\psi}, \quad \boldsymbol{\psi} = \{111000\}^T \\ \mathbf{u}^* : \text{in-plane Y-periodic} \end{cases} \quad (6)$$

where $\boldsymbol{\sigma}(\mathbf{y})$ is the microscopic stress, \mathbf{w} is the microscopic displacement, and $\boldsymbol{\varepsilon}^{\text{th}}$ is the microscopic thermal strain, with ΔT being the temperature change. Here, \mathbf{C} is a standard matrix for storing elastic constants, and α is the coefficient of thermal expansion (CTE) used for the in-plane unit cell. With macroscopic excitations $\tilde{\mathbf{E}}$ and ΔT given as input data in addition to the material constants, the governing equations must be solved for the unknown fluctuating displacement field \mathbf{u}^* under the in-plane periodic boundary conditions.

Conversely, generalized macroscopic stress is defined as

$$\tilde{\mathbf{M}} = \int_{-h/2}^{h/2} \mathbf{z}^T \left(\frac{1}{l_1 l_2} \int_{-l_1/2}^{l_1/2} \int_{-l_2/2}^{l_2/2} \boldsymbol{\sigma} dy_1 dy_2 \right) dz_3 = \int_{-h/2}^{h/2} \mathbf{z}^T \boldsymbol{\Sigma} dz_3 \quad (7)$$

where z_3 has replaced y_3 , and the following definition is applied under the assumption that $\boldsymbol{\sigma}$ is independent of $z_i (i = 1, 2)$:

$$\boldsymbol{\Sigma}(z_3) = \frac{1}{A} \int_{-l_1/2}^{l_1/2} \int_{-l_2/2}^{l_2/2} \boldsymbol{\sigma}(y_1, y_2, z_3) dy_1 dy_2 \quad (8)$$

where $A = l_1 l_2$ is the in-plane cross-sectional area. Here, components $-z_1/2$ and $-z_2/2$ of $\tilde{\mathbf{z}}$ have disappeared in z [25]. Simultaneously, the equation relating generalized macroscopic stress and strain is recognized as

$$\tilde{\mathbf{M}} = \tilde{\mathbf{D}} \left(\tilde{\mathbf{E}} - \Delta T \tilde{\mathbf{E}}^{\text{th}} \right) = \tilde{\mathbf{D}} \tilde{\mathbf{E}} - \Delta T \tilde{\mathbf{M}}^{\text{th}} \tag{9}$$

where $\tilde{\mathbf{D}}$ is the homogenized plate stiffness matrix. Here, $\tilde{\mathbf{E}}^{\text{th}}$ and $\tilde{\mathbf{M}}^{\text{th}}$ are the generalized macroscopic thermal strain and stress per unit temperature change, respectively.

In this study, the components of $\tilde{\mathbf{D}}$ and $\tilde{\mathbf{M}}^{\text{th}}$ are obtained by conducting NPTs independently, each of which corresponds to the process of solving the microscopic BVP (6). Please refer to Appendix A for details concerning the NPT.

2.2. Incorporation of co-rotational formulation

In this section, the CR formulation is introduced, to enable consideration of the large rotations that occur during the in-plane homogenization analyses performed with the local coordinate system attached to each plate element.

In the CR formulation, the total motion of each FE is decomposed into rigid body motion and pure deformation. For this decomposition, we define three separate configurations as illustrated in Figure 5, namely, initial, CR, and deformed configurations. Here, the CR configuration, located midway between the initial and deformed configurations, is a virtual configuration that undergoes rigid body motions only. Therefore, the motion from CR to deformed configurations becomes a pure deformation that can be either finite or infinitesimal. In this study, a linearly elastic material is assumed for the pure deformation in the CR coordinate system within the small strain framework. Under this assumption, the NPT presented in the previous section, and in Appendix A, can be conducted without any modification of the CR configuration of each element.

As depicted in Figure 5, each configuration has its own coordinate system. The local coordinate system $C-\bar{x}_1\bar{x}_2\bar{x}_3$ embedded in the CR configuration is denoted the CR coordinate system because these systems co-rotate. Here, rotation matrix \mathbf{R}^0 is applied to rotate the initial configuration, with its coordinate system $C^0-\bar{x}_1^0\bar{x}_2^0\bar{x}_3^0$, to the CR configuration. The coordinate transformations from the global coordinate system to the initial and CR coordinate systems are then realized using transformation matrices \mathbf{T}^0 and \mathbf{T} , respectively, so that each elemental internal force vector and tangent stiffness matrix computed for the CR configuration are transformed to the global coordinate system.

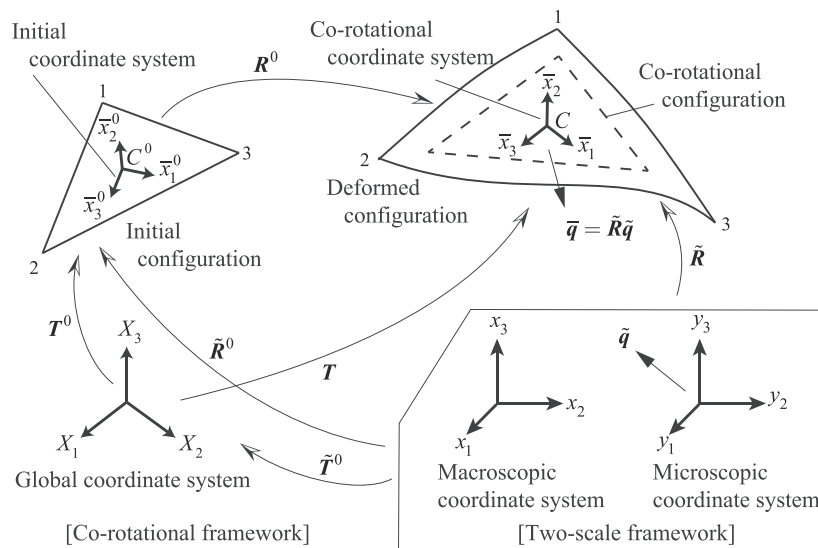


Figure 5. Configurations with global and local coordinate systems in co-rotational formulation.

The aforementioned setting is common to the CR framework but must be properly linked with the two-scale framework to accommodate the two-scale plate model with NPTs. To do this, the relationship between the CR coordinate system and the microscale coordinate system for NPTs, which normally is assumed to be consistent with the macroscale coordinate system, must be defined first. Because the orientation of an initial coordinate system is automatically generated in accordance with the numbering of element nodes in the CR formulation implementation, we first define the positional relationship between the microscale and global coordinate systems with transformation matrix \tilde{T}^0 . The transformation from the microscale to initial coordinate systems then can be recognized as $\tilde{\mathbf{R}}^0 = \mathbf{T}^0 \tilde{T}^0$. Accordingly, we transform vector $\tilde{\mathbf{q}}$, defined in the microscale coordinate system as $\tilde{\mathbf{q}}^0 = \tilde{\mathbf{R}}^0 \tilde{\mathbf{q}}$ in the initial coordinate system. Because $\tilde{\mathbf{q}} = \mathbf{R}^0 \tilde{\mathbf{q}}^0$, the transformation from the microscopic to CR coordinate systems is given by

$$\tilde{\mathbf{q}} = \tilde{\mathbf{R}} \tilde{\mathbf{q}} \quad (10)$$

where $\tilde{\mathbf{q}}$ is a vector in the CR coordinate system and the transformation matrix is defined as $\tilde{\mathbf{R}} = \mathbf{R}^0 \tilde{\mathbf{R}}^0$.

Thus, the computations applied to the actual elements in the present two-scale CR framework begin by evaluating the internal force vector $\tilde{\mathbf{f}}_e$ for each plate element in the microscale coordinate system produced by the generalized elastic displacement vector $\tilde{\mathbf{p}}^e = \{\tilde{\mathbf{u}}^e, \tilde{\boldsymbol{\theta}}^e\}$ and temperature change, expressed as

$$\tilde{\mathbf{f}}_e = \tilde{\mathbf{k}}_e \tilde{\mathbf{p}}^e - \tilde{\mathbf{f}}_e^{\text{th}} \quad (11)$$

where the element stiffness matrix $\tilde{\mathbf{k}}_e$ and thermal force vector $\tilde{\mathbf{f}}_e^{\text{th}}$ are respectively defined with

$$\tilde{\mathbf{k}}_e = \int \tilde{\mathbf{B}}^T \tilde{\mathbf{D}} \tilde{\mathbf{B}} d\Omega_{\text{ele}} \quad (12)$$

$$\tilde{\mathbf{f}}_e^{\text{th}} = \int \Delta T \tilde{\mathbf{B}}^T \tilde{\mathbf{M}}^{\text{th}} d\Omega_{\text{ele}} \quad (13)$$

Here, $\tilde{\mathbf{D}}$ is the homogenized plate stiffness matrix, and $\tilde{\mathbf{B}}$ is the translation matrix from the generalized elastic displacement vector into the generalized strain vector, $\tilde{\mathbf{E}} = \tilde{\mathbf{B}} \tilde{\mathbf{p}}^e$.

Using the relationship in (10), we have the internal force vector in the CR coordinate system as

$$\tilde{\mathbf{f}}_e = \tilde{\mathbf{R}} \tilde{\mathbf{f}}_e = \tilde{\mathbf{R}} (\tilde{\mathbf{k}}_e \tilde{\mathbf{p}}^e - \tilde{\mathbf{f}}_e^{\text{th}}) = \tilde{\mathbf{R}} \tilde{\mathbf{k}}_e (\tilde{\mathbf{R}}^T \tilde{\mathbf{p}}^e) - \tilde{\mathbf{R}} \tilde{\mathbf{f}}_e^{\text{th}} = (\tilde{\mathbf{R}} \tilde{\mathbf{k}}_e \tilde{\mathbf{R}}^T) \tilde{\mathbf{p}}^e - \tilde{\mathbf{R}} \tilde{\mathbf{f}}_e^{\text{th}} = \bar{\mathbf{k}}_e \tilde{\mathbf{p}}^e - \bar{\mathbf{f}}_e^{\text{th}} \quad (14)$$

where $\tilde{\mathbf{p}}^e = \tilde{\mathbf{R}} \tilde{\mathbf{p}}^e$, $\bar{\mathbf{k}}_e = \tilde{\mathbf{R}} \tilde{\mathbf{k}}_e \tilde{\mathbf{R}}^T$ and $\bar{\mathbf{f}}_e^{\text{th}} = \tilde{\mathbf{R}} \tilde{\mathbf{f}}_e^{\text{th}}$. Thus, the element stiffness matrix in the CR coordinate system can be computed as

$$\bar{\mathbf{k}}_e = \int \tilde{\mathbf{R}} \tilde{\mathbf{B}}^T \tilde{\mathbf{D}} \tilde{\mathbf{B}} \tilde{\mathbf{R}}^T d\Omega_{\text{ele}} = \int \bar{\mathbf{B}}^T \tilde{\mathbf{D}} \bar{\mathbf{B}} d\Omega_{\text{ele}} \quad (15)$$

where we have defined $\bar{\mathbf{B}} = \tilde{\mathbf{B}} \tilde{\mathbf{R}}^T$.

To obtain the internal force vector in the global coordinate system, we postulate that the virtual work in both the global and CR coordinate systems are conjugate, such that

$$\delta \mathbf{d}^T \mathbf{f}_e = \delta \tilde{\mathbf{p}}^e{}^T \tilde{\mathbf{f}}_e \quad (16)$$

The generalized (virtual) elastic displacement vector in the CR framework, described in detail in Appendix B, is related to the global coordinate system as

$$\delta \tilde{\mathbf{p}}^e = \boldsymbol{\Lambda} \delta \mathbf{d} \quad (17)$$

Thus, for any $\delta \mathbf{d}$, Equation (16) becomes

$$\delta \mathbf{d}^T \mathbf{f}_e = \delta \mathbf{d}^T \boldsymbol{\Lambda}^T \tilde{\mathbf{f}}_e \quad (18)$$

which yields the following relationship between the internal force vectors in the global and CR coordinate systems:

$$\mathbf{f}_e = \mathbf{\Lambda}^T \bar{\mathbf{f}}_e \quad (19)$$

A consistent tangent stiffness is established by linearizing this equation with respect to the generalized total displacement vector $\delta \mathbf{d}$, with

$$\delta \mathbf{f}_e = \mathbf{k}_T^e \delta \mathbf{d} \quad (20)$$

where \mathbf{k}_T^e is the element tangent stiffness matrix whose derivation is detailed in the literature; see, for example, [31, 33].

3. TWO-SCALE TOPOLOGY OPTIMIZATION PROBLEMS

In this section, after introducing design variables such as those used in standard or single-scale topology optimization, we present two individual two-scale topology optimization problems. Sensitivity analyses of the objective functions and the homogenized quantities are then conducted for both problems. Finally, the accuracy of the derived sensitivities is verified by comparison with sensitivities evaluated through numerical differentiations.

3.1. Design variables and effective material parameters for in-plane unit cell

Assuming that the in-plane unit cell consists of two different materials and that spatial discretization with FEs is completed, we choose the volume fraction for one of the materials for FE i as design variable s_i , with range $0 \leq s_i \leq 1$. Then, using a developed optimization algorithm, the material distribution of the in-plane unit cell is updated by changing values of s_i to maximize the macroscopic mechanical performance. In this context, the microscopic stress $\boldsymbol{\sigma}$ evaluated using the second equation of (6) is rewritten as

$$\boldsymbol{\sigma}(s) = \mathbf{C} (\boldsymbol{\varepsilon} - \boldsymbol{\varepsilon}^{\text{th}}) = \bar{\mathbf{C}} (E^0(s)\boldsymbol{\varepsilon}(s) - \beta(s)\Delta T\boldsymbol{\psi}) \quad (21)$$

where E^0 is Young's modulus, $\beta = \alpha E^0$ is the coefficient of thermal stress (CTS) [34], and $\bar{\mathbf{C}} = \mathbf{C}/E^0$ is the elasticity matrix independent of E^0 .

Young's modulus E^0 and the CTS β are then defined as functions of design variable s_i in element i . More specifically, employing the RAMP method [34, 35], we introduce the following nonlinear interpolation functions for the effective Young's modulus and the effective CTS, both of which vary with s_i :

$$E^0(s_i) = \left(1 - \frac{s_i}{1 + q_{E^0}(1 - s_i)}\right) E_1^0 + \left(\frac{s_i}{1 + q_{E^0}(1 - s_i)}\right) E_2^0 \quad (22)$$

$$\beta(s_i) = \left(1 - \frac{s_i}{1 + q_\beta(1 - s_i)}\right) \beta_1 + \left(\frac{s_i}{1 + q_\beta(1 - s_i)}\right) \beta_2 \quad (23)$$

where E_1^0 and β_1 are the Young's modulus and CTS of Phase I, respectively. Here, q_{E^0} and q_β are penalty parameters independent of the underlying physical phenomena. The combination of these parameters in the RAMP method has been explored in depth in Reference [34], which concludes that the set of $q_{E^0} = 8$ and $q_\beta = 0$ makes optimization calculations stable for thermo-mechanical optimization problems. Because the same empirical evidence was found during this study, these values are employed for the calculations in the following sections.

3.2. Optimization problems

Two two-scale topology optimization problems are now presented, one to maximize the macroscopic stiffness of a composite plate and the other to maximize the macroscopic displacements at prescribed nodes.

3.2.1. *Problem I: In-plane unit cell that maximizes macroscopic stiffness.* To determine an in-plane unit cell that maximizes the macroscopic overall stiffness, we formulate the following optimization problem by defining specific objective and constraint functions:

$$\min f(\mathbf{s}) = \mathbf{F}_{\text{ext}}^T \mathbf{U}(\mathbf{s}) \quad (24)$$

$$\text{subject to } h(\mathbf{s}) = \sum_{i=1}^{n_{\text{elem}}} s_i v_i - V_0 = 0 \quad (25)$$

Here, $\mathbf{U}(\mathbf{s})$ is the generalized (global) macroscopic nodal displacement vector, and \mathbf{F}_{ext} is the generalized (global) macroscopic nodal (external) force vector. Also, n_{elem} is the total number of FEs, and v_i is the volume of element i . The minimization of objective function $f(\mathbf{s})$ representing the macroscopic end compliance is equivalent to maximization of the macroscopic overall stiffness in this case. Additionally, equality constraint $h(\mathbf{s})$ in Equation (25) requires the total volume of Phase 2 in the in-plane unit cell to be identical to the prescribed value V_0 . Temperature changes are not considered in this optimization problem.

3.2.2. *Problem II: In-plane unit cell that maximizes specific nodal displacements.* By using macroscopic quasi-end-compliance as an objective function, we formulate an optimization problem to maximize certain nodal displacements of the macroscopic plate under thermal loading attributable to ΔT , as

$$\min f(\mathbf{s}) = \mathbf{F}^v T \mathbf{U}(\mathbf{s}) \quad (26)$$

along with constraint (25). Here, \mathbf{U} is the generalized macroscopic nodal displacement vector, and \mathbf{F}^v is the virtual force vector, in which only selected components of F_k^v have non-zero values, whereas the others are zero:

$$\mathbf{U}(\mathbf{s}) = (U_1, U_2, \dots, U_k, \dots)^T \quad (27)$$

$$\mathbf{F}^v = (F_1^v, F_2^v, \dots, F_k^v, \dots)^T = (0, 0, \dots, F_k^v, 0, \dots)^T \quad (28)$$

3.2.3. *Optimization calculation schemes.* For gradient-based topology optimization problems, two optimization algorithms, namely, the optimality criterial (OC) method [36] and the method of moving asymptotes [37], are generally used. The OC is employed for Problem I (stiffness maximization problem) because the objective function itself is a ‘monotonously increasing/decreasing function’ for any design variable and the constraint is represented by a linear function. It is indeed known that the OC method is effective to solve this kind of optimization problems and provides reliable optimization results with fast convergence. On the contrary, we apply method of moving asymptotes for Problem II because the objective function is not necessarily monotonously varying; this is a typical condition for topology optimization to maximize/minimize mean compliance of a structure subjected to thermal expansion or self-weight. With this background, the equality constraint (25) is converted to an inequality condition that must be satisfied within a small error range.

To suppress checkerboarding in optimized topologies, a particular filtering technique must be applied. In this study, the sensitivity of each element is replaced by the weighted-average of sensitivities of adjacent elements [38] as

$$\frac{\partial \tilde{f}^*(\mathbf{s})}{\partial s_i} = \frac{\sum_{j=1}^{n_{\text{elem}}} \frac{1}{v_j} w_{ij} s_j \frac{\partial f^*}{\partial s_j}}{\sum_{j=1}^{n_{\text{elem}}} \frac{1}{v_j} w_{ij} s_j} \quad (29)$$

where i and j are element numbers. Here, we have introduced $w_{ij} = \exp \left[-\frac{1}{2} \left(\frac{r_{ij}}{r^0/2} \right)^2 \right]$ as a weight of j for element i [39], in which r_{ij} is the distance between the centers of elements i and j , and r^0

defines the domain of filtering. This filter has widely been utilized because of its usability, although it has no theoretical underpinning [38, 40]. Better optimization results could be obtained if we utilize theoretically proven and hence more reliable filters such as a class of ‘density filters’; see early developments in [27, 41] and more recently proposed ones in [42]. This point must be an issue to be addressed in the future.

It should also be noted that the framework of the proposed two-scale topology optimization is almost the same as that introduced by Kato *et al.* [12], except that microscopic analyses, or equivalently NPTs, must be conducted for in-plane unit cells instead of for unit cells with 3D periodicity. Therefore, the computer implementation requires few modifications relevant to in-plane homogenization. In addition, the two-scale optimization algorithm itself guarantees low-computational cost because of the method of multi-scale decoupling analysis [13]. However, microscopic analyses in the iterative procedure used in this method requires more computational cost than those of [12], because constraints (A7) for NPT imply that the microscopic stiffness matrices become dense; see Reference [25]. Nonetheless, computational cost required in the proposed two-scale topology optimization method is substantially smaller than that based on multi-scale coupling analysis.

3.3. Sensitivity analyses

Using the adjoint method, we now present the analytical sensitivities of the objective functions introduced in the aforementioned optimization problems, along with the homogenized quantities with respect to design variable s_i .

3.3.1. Sensitivities of objective functions. First, the objective function in Equation (25) for Problem I is replaced with an equivalent function f^* as follows:

$$f^*(s) = \mathbf{F}_{\text{ext}}^T \mathbf{U}(s) - \lambda^T \mathbf{r}(s) \quad (30)$$

where λ is an arbitrarily chosen adjoint vector and \mathbf{r} is the macroscopic residual vector. Here, \mathbf{r} is intended to satisfy the equilibrium condition $\mathbf{r} = \mathbf{F}_{\text{ext}} - \mathbf{F}_{\text{int}} = 0$. In addition, \mathbf{F}_{int} is the global macroscopic internal force vector assembled from the internal force vectors \mathbf{f}_e of all the elements defined in Equation (19). Differentiation of Equation (30) with respect to design variable s_i yields

$$\begin{aligned} \frac{\partial f^*(s)}{\partial s_i} &= \frac{d\mathbf{F}_{\text{ext}}^T}{ds_i} \mathbf{U} + \mathbf{F}_{\text{ext}}^T \frac{\partial \mathbf{U}}{\partial s_i} - \lambda^T \frac{d\mathbf{r}}{ds_i} \\ &= \mathbf{F}_{\text{ext}}^T \frac{\partial \mathbf{U}}{\partial s_i} - \lambda^T \left(\frac{\partial \mathbf{r}}{\partial \mathbf{U}} \frac{\partial \mathbf{U}}{\partial s_i} + \frac{\partial \mathbf{r}}{\partial s_i} \right) \\ &= (\mathbf{F}_{\text{ext}}^T - \lambda^T \mathbf{K}_T) \frac{\partial \mathbf{U}}{\partial s_i} - \lambda^T \frac{\partial \mathbf{r}}{\partial s_i} \end{aligned} \quad (31)$$

where \mathbf{K}_T is the macroscopic global tangent stiffness matrix, which is symmetric, assembled from the element tangent stiffness matrices \mathbf{k}_T^e defined in Equation (20). Here, we have assumed that the external loading is independent of the design variables so that $d\mathbf{F}_{\text{ext}}^T/ds_i$ vanishes. Because the adjoint vector λ can accommodate arbitrary components, we can satisfy the following equation:

$$\mathbf{F}_{\text{ext}} = \mathbf{K}_T \lambda \quad (32)$$

which eliminates the first term of Equation (31). Thus, Equation (31) yields

$$\frac{\partial f^*(s)}{\partial s_i} = -\lambda^T \frac{\partial \mathbf{r}(s)}{\partial s_i} \quad (33)$$

Because only the homogenized plate stiffness for the internal force vector $\bar{k}_e \bar{p}^e$ in Equation (14) explicitly depend on design variable s_i in $\partial \mathbf{r} / \partial s_i$, the sensitivity of $\partial \mathbf{r} / \partial s_i$ can be computed as

$$\frac{\partial \mathbf{r}(s)}{\partial s_i} = \frac{\partial \mathbf{F}^{\text{int}}}{\partial s_i} = A_{e=1} \int \frac{\partial \mathbf{f}_e}{\partial s_i} d\Omega = \int \Lambda^T \mathbf{B}^{-T} \frac{\partial \bar{\mathbf{D}} \bar{\mathbf{B}} \bar{p}^e}{\partial s_i} d\Omega \quad (34)$$

where Equations (15) and (19) are utilized. Note that $A_{e=1}$ indicates the assembly operator.

The sensitivity of the objective function (26) in Problem II can also be derived in a similar manner, with an adjoint vector that satisfies the following equation:

$$\mathbf{F}^v = \mathbf{K}_T \lambda \quad (35)$$

The only difference is that thermal force vector \tilde{f}_e^{th} in Equation (14) is now involved such that

$$\frac{\partial \mathbf{r}(s)}{\partial s_i} = \int \Lambda^T \mathbf{B}^{-T} \left(\frac{\partial \bar{\mathbf{D}} \bar{\mathbf{B}} \bar{p}^e}{\partial s_i} - \Delta T \frac{\partial \bar{\mathbf{M}}^{\text{th}}}{\partial s_i} \right) d\Omega \quad (36)$$

3.3.2. Sensitivity of homogenized plate stiffness matrix and generalized thermal strain. By multiplying the homogenized plate stiffness matrix by the generalized macroscopic strain vector whose b -th component has a value of one while the other component values are zero, denoted $\tilde{\mathbf{E}}^b$, we can compute the b -th column vector. Next, component $D_{a,b}$ is obtained via the inner product between the b -th column vector and the generalized macroscopic strain vector whose a -th component has a value of one while the other components are zero, denoted $\tilde{\mathbf{E}}^a$. Thus, we have

$$\tilde{D}_{ab}(s) = \left(\tilde{\mathbf{E}}^a \right)^T \tilde{\mathbf{D}} \tilde{\mathbf{E}}^b \quad (37)$$

$$\tilde{\mathbf{E}}^a = \{ \tilde{E}^1 \dots \tilde{E}^a \dots \tilde{E}^8 \}^T = \{ 0 \dots 1 \dots 0 \}^T \quad (38)$$

$$\tilde{\mathbf{E}}^b = \{ \tilde{E}^1 \dots \tilde{E}^b \dots \tilde{E}^8 \}^T = \{ 0 \dots 1 \dots 0 \}^T \quad (39)$$

In view of Equations (4), (7), and (9), $\tilde{D}_{a,b}$ in Equation (37) can be expressed with the microscopic strain and stress as

$$\begin{aligned} \tilde{D}_{ab}(s) &= \frac{1}{A} \left(\tilde{\mathbf{E}}^a \right)^T \int_Y \mathbf{z}^T \boldsymbol{\sigma}^{(b)} dY \\ &= \frac{1}{A} \int_Y (\boldsymbol{\varepsilon}^{(a)} - \partial_y \mathbf{u}^*)^T \boldsymbol{\sigma}^{(b)} dY \\ &= \frac{1}{A} \int_Y \boldsymbol{\varepsilon}^{(a)T} \mathbf{C} \boldsymbol{\varepsilon}^{(b)} dY \end{aligned} \quad (40)$$

Here, we have utilized the microscopic equilibrium equation $\int_V \partial_y \mathbf{u}^{*T} \boldsymbol{\sigma}^{(b)} dV = 0$ under the condition $\Delta T = 0$. In Equation (40), $\boldsymbol{\varepsilon}^{(a)}$ and $\boldsymbol{\varepsilon}^{(b)}$ are the microscopic strain vectors obtained as solutions of the governing equation, (6), with the aforementioned generalized macroscopic strains $\mathbf{E}^{(a)}$ and $\mathbf{E}^{(b)}$ used as data. Based on the aforementioned equations, derivatives of the components of the homogenized stiffness matrix $\partial \tilde{D}_{ab}(s_i) / \partial s_i$ are now derived as

$$\begin{aligned} \frac{\partial \tilde{D}_{ab}(s)}{\partial s_i} &= \frac{1}{A} \int_V \boldsymbol{\varepsilon}^{(a)T} \frac{\partial \mathbf{C}}{\partial s_i} \boldsymbol{\varepsilon}^{(b)} dV + \frac{1}{A} \int_V \frac{\partial \boldsymbol{\varepsilon}^{(a)T}}{\partial s_i} \mathbf{C} \boldsymbol{\varepsilon}^{(b)} dV + \frac{1}{A} \int_V \boldsymbol{\varepsilon}^{(a)T} \mathbf{C} \frac{\partial \boldsymbol{\varepsilon}^{(b)}}{\partial s_i} dV \\ &= \frac{1}{A} \int_V \boldsymbol{\varepsilon}^{(a)T} \frac{\partial \mathbf{C}}{\partial s_i} \boldsymbol{\varepsilon}^{(b)} dV \end{aligned} \quad (41)$$

given that $\partial \epsilon / \partial s_i = \partial (\partial_y \mathbf{u}^*) / \partial s_i$. Thus, the analytical sensitivity of $\tilde{\mathbf{D}}$ with respect to s_i becomes

$$\frac{\partial \tilde{D}_{ab}(s)}{\partial s_i} = \frac{1}{A} \int_V \epsilon^{(a)\top} \frac{\partial E^0}{\partial s_i} \bar{\mathbf{C}} \epsilon^{(b)} dV \quad (42)$$

The sensitivity of the generalized thermal stress can also be derived in a similar manner. With the components of the generalized thermal stress vector $\tilde{\mathbf{M}}_a^{\text{th}}$ expressed as

$$\tilde{\mathbf{M}}_a^{\text{th}}(s) = \left(\tilde{\mathbf{E}}^{(a)} \right)^\top \tilde{\mathbf{M}} = \frac{1}{A} \int_V \epsilon^{(a)\top} \mathbf{C} \left(\epsilon^{(\text{th})} - \beta \bar{\mathbf{C}} \boldsymbol{\psi} \right) dV \quad (43)$$

the analytical sensitivities of the a components of $\partial \tilde{\mathbf{M}}^{\text{th}}(s) / \partial s_i$ become

$$\frac{\partial \tilde{M}_a^{\text{th}}(s)}{\partial s_i} = \frac{1}{A} \int_V \epsilon^{(a)\top} \left(\frac{\partial E^0}{\partial s_i} \bar{\mathbf{C}} \epsilon^{(\text{th})} - \frac{\partial \beta}{\partial s_i} \bar{\mathbf{C}} \boldsymbol{\psi} \right) dV \quad (44)$$

where $\epsilon^{(\text{th})}$ is the microscopic strain obtained as a solution for governing Equation (6), with the data expressed in (A6) that uses NPTs to evaluate the generalize macroscopic thermal strain.

4. NUMERICAL EXAMPLES

In this section, we present several numerical examples for Problems I and II, which are defined in the previous section, to demonstrate the potential of the proposed two-scale topology optimization method for the design of composite plates with in-plane periodicity.

4.1. Problem I: Maximization of macroscopic stiffness

Let us determine a single optimal topology of an in-plane unit cell that maximizes the macroscopic stiffness of the overall composite plate structure. Because the proposed two-scale topology optimization method is based on in-plane homogenization, the asymmetry of the material distribution in an in-plane unit cell activates the coupling between the transverse shear and the in-plane/out-of-plane deformations, as demonstrated in Reference [25]. Additionally, because large rotations of the macroscopic plate are allowed, the optimal topology is expected to depend on the amount of macroscopic deformation. To illustrate the unique features of the proposed method, we define the macroscopic problem illustrated in Figure 6 and conduct two cases with different loading parameters, $\mu = 1.0 \times 10^5$ and $\mu = 8.0 \times 10^8$, which correspond to small and large rotations, respectively. We note that the macrostructure can be classified as a thick plate because the ratio of the thickness to the axial length is 0.1. Bending about the x_2 -axis and the transverse shear in the $x_1 x_3$ -plane is therefore predominant compared with other deformations. In this numerical example, the in-plane unit

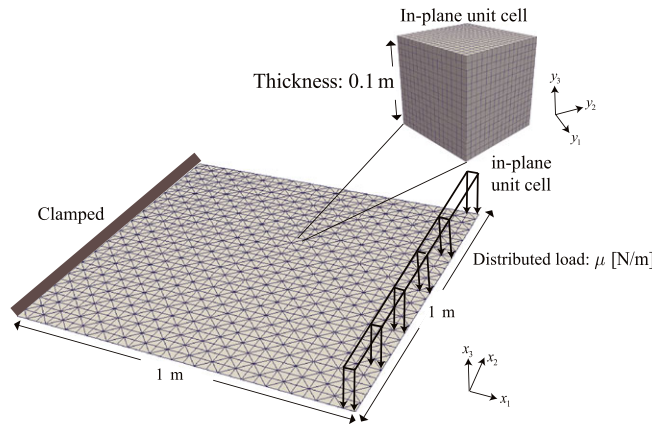


Figure 6. Finite element mesh and boundary conditions for Problem I.

cell is cubic and composed of a single material whose Young's modulus and Poisson's ratio are set at 1.0×10^{10} and 0.3, respectively, and its FE model is composed of $16 \times 16 \times 16$ 3D cubic solid elements that have 14,739 degrees-of-freedom (DOFs). However, the macrostructure is composed of 1800 three-node triangular flat-shell elements and has 5766 DOFs. Moreover, the radius of filtering presented in Equation (29) is set at $r_0 = 0.01$ that is one-tenth of one side of the in-plane unit cell.

The obtained optimal topologies for the two loading cases are shown in Figure 7. Here, the design variables are converted as elemental values to nodal values so that smooth iso-surfaces are visualized by standard visualization software. In both of the obtained in-plane unit cell topologies, material is distributed in the upper and bottom portions, causing the composite plate resist bending deformations, and diagonal members in the x_1x_3 -plane are formed that create resistance to transverse shear deformations. At first glance, they are similar to each other in terms of topological feature. However, differences in certain components of the homogenized plate stiffness matrices obtained from the optimal in-plane unit cells, as listed in Table I, can be recognized. Here, the upper indices of \tilde{D}^S and \tilde{D}^L indicate those obtained for the small and large rotation cases, respectively. In particular, their (1, 4) components, which indicate the degree of coupling between the in-plane strain \tilde{E}_1 and curvature \tilde{E}_4 , differ substantially. Furthermore, there is a noticeable difference between the (1, 8) components, which reflect the coupling between the membrane force \tilde{M}_1 and the transverse shear strain \tilde{E}_8 . More specifically, these components in the large rotation case have larger values than those of the small rotation case. This is probably because that the bending and transverse shear deformations caused by the membrane force, which are increased in the plate subjected to large rotation, must be suppressed. Figure 8 shows the convergence history of the normalized objective functions with respect to the number of iterations for these optimization calculations, both of which exhibit the convergences with approximately 500 iterations.

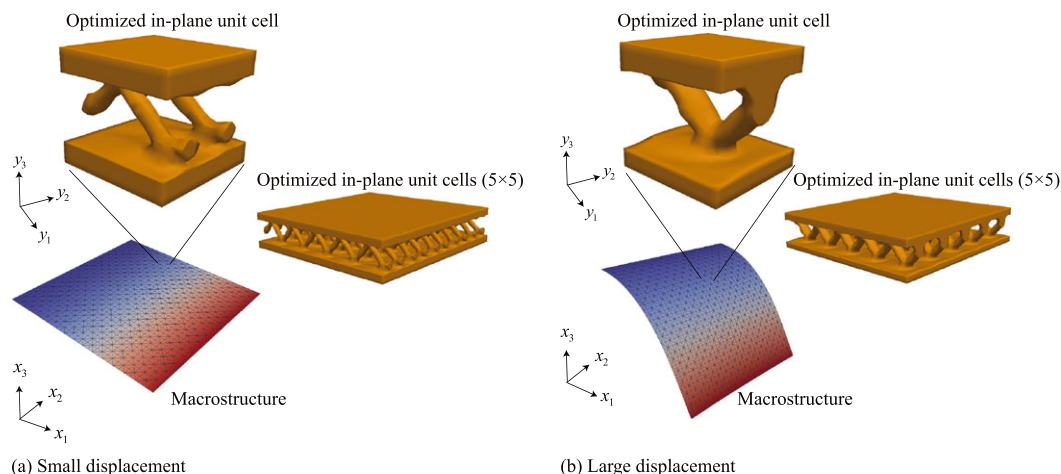


Figure 7. Optimal topologies for Problem I.

Table I. Selected stiffnesses of optimal in-plane unit cell.

Components (a, b)	$\tilde{D}_{a,b}^L$	$\tilde{D}_{a,b}^S$
$\tilde{D}_{1,1}$ [N/m]	4.07×10^8	4.32×10^8
$\tilde{D}_{1,4}$ [N]	-1.28×10^6	-2.75×10^4
$\tilde{D}_{4,4}$ [N·m]	6.72×10^5	7.07×10^5
$\tilde{D}_{1,8}$ [N]	-1.28×10^6	-6.66×10^5
$\tilde{D}_{8,8}$ [N/m]	1.44×10^7	1.14×10^7

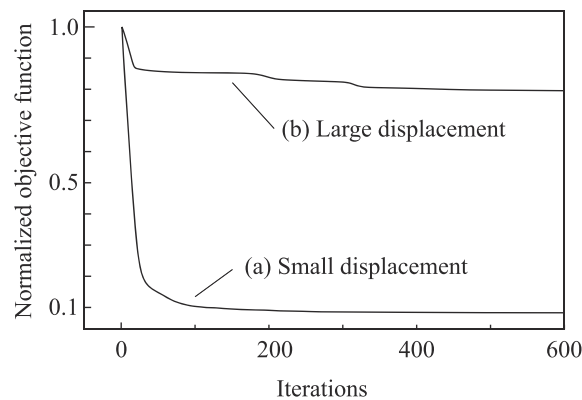


Figure 8. Iteration history of the normalized objective function.

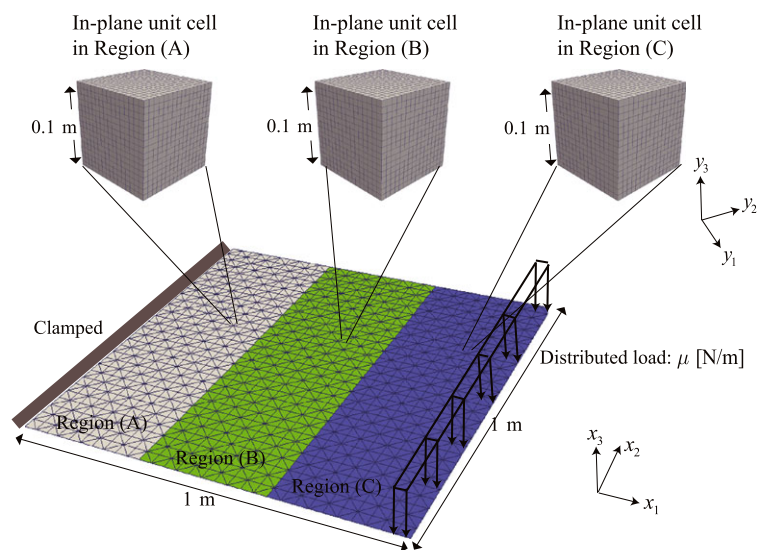


Figure 9. Finite element mesh with three regions to assign separate in-plane unit cells for Problem I.

To confirm the aforementioned points, we considered a macrostructure in which in-plane unit cells were separately assigned to three specified regions, designated Regions (A), (B), and (C), as shown in Figure 9, and solved the same set of optimization problems as before. The obtained optimal topologies for the cases of small and large rotation are presented in Figures 10 and 11, respectively. As these figures illustrate, the optimized topologies of the in-plane unit cells in Regions (A) and (B) are similar for both rotation cases, but those of the in-plane unit cells in Region (C) are markedly different. Whereas the Region (C) optimal topology obtained for the small rotation case has a simple wall member that resists the transverse shear deformation, that of the large rotation case has a more complex and asymmetric structure with respect to both the y_1y_2 and y_2y_3 planes. This asymmetric material distribution acts to couple the components of the homogenized plate stiffness matrix. Indeed, as the data in Table II indicate, the in-plane unit cell in Region (C) yields relatively large values in the components representing the coupling of the in-plane membrane strain \tilde{E}_1 for both bending and transverse shear deformations, \tilde{E}_4 and \tilde{E}_8 . Thus, the bending and transverse shear deformations induced by the in-plane membrane stress seems to effectively increase the overall stiffness of the macroscopic plate in this case for large rotation. To confirm the effectiveness of this increase, we conducted two separate macroscopic analyses with loading parameter $\mu = 8.0 \times 10^8$ (the previous large rotation setting) using the homogenized plate stiffness matrices \tilde{D}^L and \tilde{D}^S obtained for

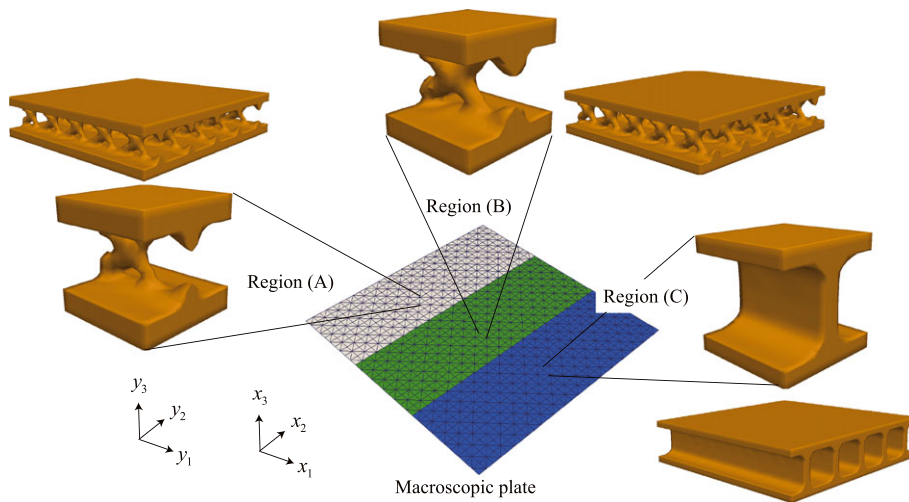


Figure 10. Three optimal topologies under small rotation setting.

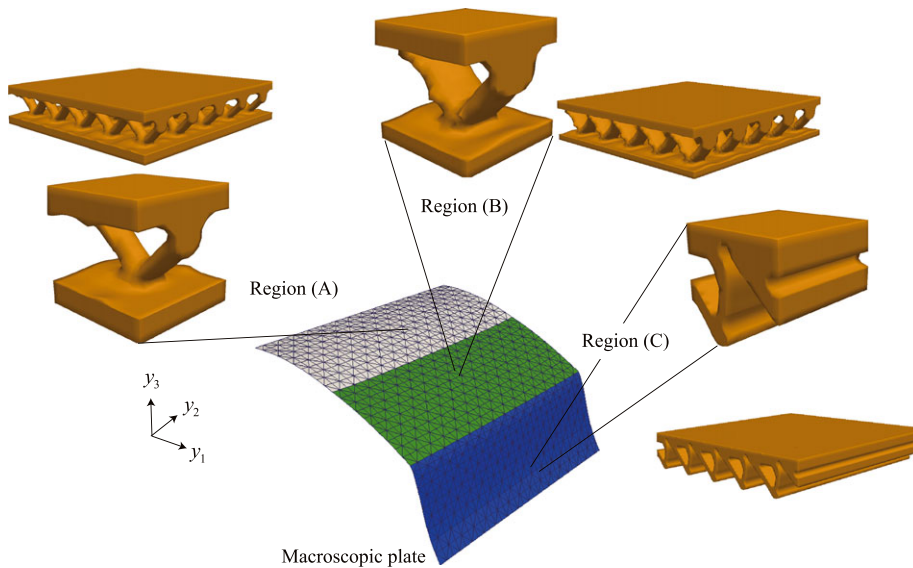


Figure 11. Three optimal topologies under large rotation setting.

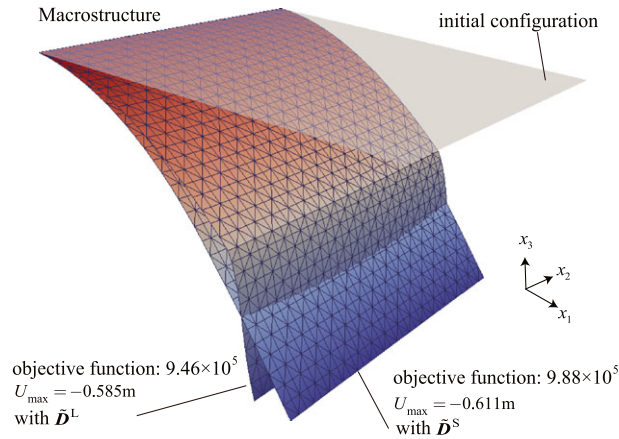
Regions (A), (B), and (C). The results appear in Figure 12 and demonstrate that the obtained optimal topologies are physically reasonable, because the deflection of the macroscopic plate with $\tilde{\mathbf{D}}^L$ is smaller than that with $\tilde{\mathbf{D}}^S$.

4.2. Problem II: Maximization of nodal displacement vector components

We now perform analyses for an optimal topology of an in-plane unit cell that maximizes selected macroscopic nodal displacements to enable adjustment of the macroscopic motion of a composite plate. The FE model of the macroscopic plate is shown in Figure 13, in which target nodes are specified. This model is composed of 600 three-node triangular flat-shell elements and has 2046 DOFs (341 nodes), whereas the FE model of the in-place unit-cell is the same as that in Problem I. In the numerical examples below, the following two cases have virtual force vectors set for the nodes of interest:

Table II. Selected stiffnesses of optimal in-plane unit cells in three separate regions.

	Components (a, b)	$\tilde{D}_{a,b}^L$	$\tilde{D}_{a,b}^S$
Region (A)	$\tilde{D}_{1,1}$ [N/m]	4.38×10^8	4.52×10^8
	$\tilde{D}_{1,4}$ [N]	1.67×10^5	1.25×10^2
	$\tilde{D}_{4,4}$ [N·m]	7.13×10^5	7.20×10^5
	$\tilde{D}_{1,8}$ [N]	-4.64×10^5	2.83×10^1
	$\tilde{D}_{8,8}$ [N/m]	9.99×10^6	7.55×10^6
Region (B)	$\tilde{D}_{1,1}$ [N/m]	3.71×10^8	4.46×10^8
	$\tilde{D}_{1,4}$ [N]	2.08×10^6	9.74×10^1
	$\tilde{D}_{4,4}$ [N·m]	6.36×10^5	7.11×10^5
	$\tilde{D}_{1,8}$ [N]	-5.69×10^5	6.03×10^3
	$\tilde{D}_{8,8}$ [N/m]	1.90×10^7	1.37×10^7
Region (C)	$\tilde{D}_{1,1}$ [N/m]	1.26×10^8	4.22×10^8
	$\tilde{D}_{1,4}$ [N]	4.86×10^6	7.98×10^2
	$\tilde{D}_{4,4}$ [N·m]	2.32×10^5	6.26×10^5
	$\tilde{D}_{1,8}$ [N]	-1.25×10^7	4.29×10^0
	$\tilde{D}_{8,8}$ [N/m]	1.06×10^7	3.25×10^7


 Figure 12. Results with \tilde{D}^L and \tilde{D}^S under large rotation condition.

$$\text{Case 1: } \mathbf{F}^{v1} = \begin{cases} -1 & (k = 1, \dots, 11 \text{ and only } z_3 \text{ direction}) \\ 0 & (\text{otherwise}) \end{cases} \quad (45)$$

$$\text{Case 2: } \mathbf{F}^{v2} = \begin{cases} 1 & (k = 1, \dots, 3 \text{ and only } z_3 \text{ direction}) \\ -1 & (k = 8, \dots, 11 \text{ and only } z_3 \text{ direction}) \\ 0 & (\text{otherwise}) \end{cases} \quad (46)$$

The FE model of the in-plane unit cell, composed of two different materials, is also depicted in Figure 14. To visualize the effect of thermal deformations, we consider two patterns of material combinations for Case 1. Patterns A and B have the material constants listed in Tables III and IV, respectively. Here, both Young's moduli and CTEs for the constituents are different for Pattern A, whereas only CTEs are different for Pattern B.

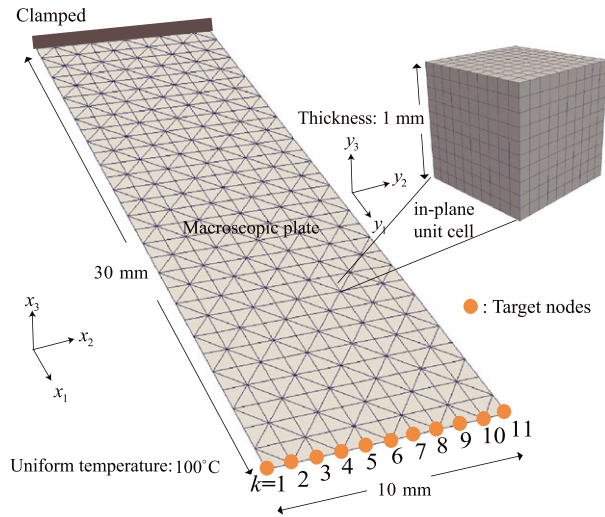


Figure 13. Finite element mesh with target nodes for Problem II.

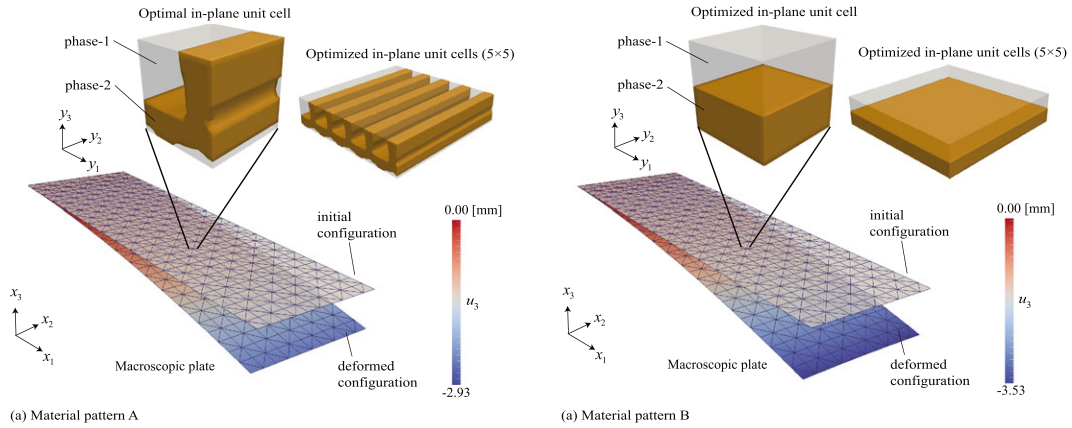


Figure 14. Optimal topologies of in-plane unit cells for Problem II: Case 1 with F^{v1} .

First, we consider Case 1 with F^{v1} , in which the deflection of the end side of the macrostructure is to be maximized. The topologies of in-plane unit cells obtained with material combinations of Patterns A and B are shown in Figure 14 and referred to as Topologies A and B, respectively. In Topology B, in which two materials have the same elastic constant, the design region is split into the upper and lower portions, with simple layering of the two materials, thus preserving the symmetries with respect to the y_2y_3 and y_3y_1 planes. Accordingly, the macroscopic thermal curvature associated with the bending about the y_2 -axis becomes non-zero ($\bar{E}_4^{th} = -2.35 [1/(mm \cdot ^\circ C)]$) and there is no coupling between the in-plane and transverse shear deformations. This result is reasonable from a mechanical viewpoint. Conversely, in Topology A, using Pattern A, a vertical member appears, although the materials are again arranged one above the other. As shown in Figure 14, the deflection with Topology A is smaller than that with Topology B.

To examine this result further, we performed another macroscopic analysis using the homogenized plate stiffness matrix and generalized thermal strain evaluated using NPTs for the in-plane unit cell of Topology B with Pattern A. In this case, the maximum absolute value of the macroscopic deflection in the x_3 -direction was $|u_3| = 2.35$ mm, smaller than that of Topology A with Pattern A ($|u_3| = 2.93$ mm). Indeed, the macroscopic thermal curvature obtained for Topology B with Pattern A was $4.87 \times 10^{-5} [1/(mm \cdot \text{celsius})]$, smaller than that of Topology A with Pattern A ($6.74 \times 10^{-5} [1/(mm \cdot \text{celsius})]$). These results imply that the macroscopic thermal strains depend on

Table III. Pattern A material combination in an in-plane unit cell for Problem II.

	Young's modulus [N/mm ²]	CTE [1/°C]	CTS [N/(mm ² · °C)]
Phase-1	1.0×10^4	5.0×10^{-5}	5.0×10^{-1}
Phase-2	1.0×10^5	1.0×10^{-5}	1.0×10^0

Table IV. Pattern B material combination in an in-plane unit cell for Problem II.

	Young's modulus [N/mm ²]	CTE [1/°C]	CTS [N/(mm ² · °C)]
Phase-1	1.0×10^5	5.0×10^{-5}	5.0×10^{-1}
Phase-2	1.0×10^5	1.0×10^{-5}	1.0×10^0

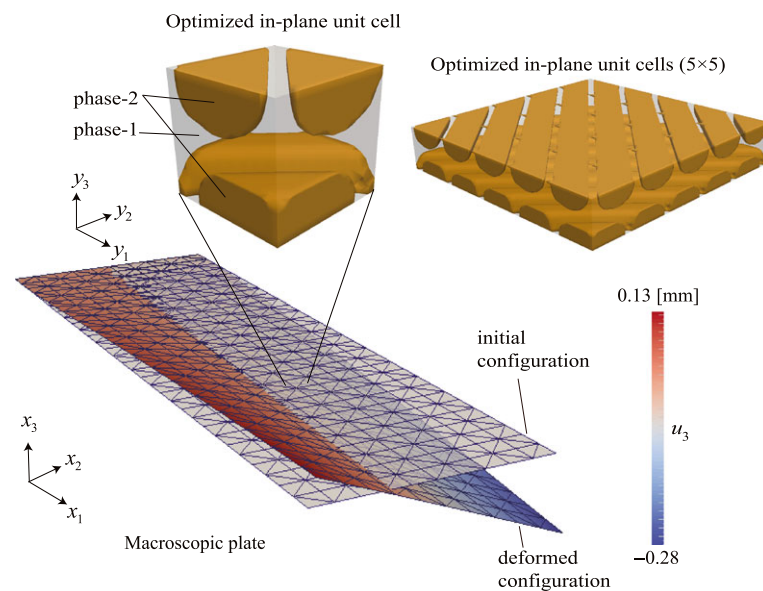


Figure 15. Optimal topology of in-plane unit cells for Problem II: Case 2 with F^{v2} .

the elastic moduli in the in-plane unit cell. More importantly, however, they suggest that Topology A subjected to the specified temperature change provides the maximum macroscopic deflection with Pattern A. In other words, when Pattern A is used, Topology A provides better results than Topology B. This may be because the maximum deflection when using Topology A with Pattern A is not only attributable to the macroscopic thermal curvature but is also influenced by the macroscopic thermal transverse shear strain caused by the asymmetric distribution of materials in the in-plane unit cell.

Next, we consider Case 2 with F^{v2} , which aims to maximize the macroscopic torsional deformation with respect to the x_1 -axis. Here, only the material combination of Pattern A is employed for the in-plane unit cell. The obtained optimal topology of the in-plane unit cell and the deformed configuration of the macroscopic plate are shown in Figure 15. As seen from the figure, Phases 1 and 2 are distributed to form a cross-ply shape in the optimal topology. The resulting in-plane unit cell has a thermal curvature associated with torsion of $\tilde{E}_6^{th} = -4.47 \times 10^{-5}$, which is the maximum value among all the components of the generalized macroscopic thermal strain. This result is sufficiently plausible from a thermo-mechanical viewpoint, given the objective of maximizing the macroscopic torsional deformation.

5. CONCLUSION

We proposed a method for two-scale topology optimization of composite plates with in-plane periodicity. This method was intended to determine an optimal in-plane unit cell that maximizes macroscopic mechanical performance. A key ingredient of this method is the NPT, based on the in-plane homogenization scheme. In the resulting two-scale composite plate model, thick plate theory is employed for the macroscopic mathematical model, whereas 3D solid mechanical behavior is realized at the microscale so that existing methods of multiscale topology optimization can be applied. To incorporate large rotations into the macroscopic plates, we employed a CR formulation that enables NPTs to be conducted within a small strain framework to evaluate homogenized plate stiffnesses and generalized thermal strains.

To showcase simple and straightforward applications of the two-scale plate model in multiscale topology optimizations, we presented two problems to determine an optimal topology in the region of an in-plane unit cell that maximizes mechanical performance. One problem aimed to maximize the macroscopic stiffness of a composite plate or equivalently, to minimize macroscopic end compliance. The second problem was to maximize the macroscopic displacement components of selected nodes to enable adjustment of macroscopic motions in response to thermo-mechanical effects. For each of these problems, the analytical sensitivities of the objective function, the homogenized plate stiffnesses, and the generalized thermal strains were derived and verified through comparisons with numerically obtained sensitivities.

Numerical examples were provided to demonstrate the effectiveness and capability of the proposed two-scale topology optimization method for designing optimal in-plane unit cells for use in composite plates. In the example problem to determine an in-plane unit cell that maximizes macroscopic stiffness, the optimized topology associated with the macroscopic plate subject to large rotations was different from that of the plate subject to small rotations because of the interaction between the in-plane and out-of-plane deformations. Furthermore, when determining optimized configurations of in-plane unit cells, each of which maximizes the macroscopic deformation in a specified direction, we obtained a variety of optimized topologies, all of which were reasonable from a thermo-mechanical standpoint.

It remains a challenge for future research to incorporate a variety of nonlinearities. In particular, incorporation of material nonlinearities would be of practical value. This should be attainable once a theory of a nonlinear NPT is sufficiently established. Methods applicable to two-scale optimization of multiphysics phenomena are also attractive subjects for future investigation.

APPENDIX A: NUMERICAL PLATE TESTING

In this appendix, we explain the method of numerical plate testing (NPT) [25] used to evaluate the homogenized plate stiffness matrix of composite plates with in-plane periodicity.

Given in-plane periodicity, the unknown variable in the governing Equation (6) for an in-plane unit cell is the microscopic displacement fluctuation \mathbf{u}^* , whereas the generalized macroscopic strain $\tilde{\mathbf{E}}$ in Equation (3) is considered a datum. However, because the displacement fluctuation \mathbf{u}^* can be expressed as

$$\begin{cases} w_1 = (\tilde{E}^1 + z_3 \tilde{E}^4) y_1 + \left(\tilde{E}^3 + \frac{z_3}{2} \tilde{E}^6 \right) \frac{y_2}{2} + \left(\tilde{E}^8 - \frac{z_2}{2} \tilde{E}^6 \right) y_3 + u_1^* \\ w_2 = \left(\tilde{E}^3 + \frac{z_3}{2} \tilde{E}^6 \right) \frac{y_1}{2} + (\tilde{E}^2 + z_3 \tilde{E}^5) y_2 + \left(\tilde{E}^7 - \frac{z_1}{2} \tilde{E}^6 \right) y_3 + u_2^* \\ w_3 = \left(\tilde{E}^8 - \frac{z_2}{2} \tilde{E}^6 \right) y_1 + \left(\tilde{E}^7 - \frac{z_1}{2} \tilde{E}^6 \right) y_2 + u_3^* \end{cases} \quad (\text{A1})$$

we eliminate \mathbf{u}^* by using the in-plane Y-periodicity condition so that the actual microscopic displacement vector \mathbf{w} becomes the unknown variable, subject to the following constraint conditions:

$$\left\{ \begin{array}{l} q_1^{[1]} \equiv w_1^{[1]} - w_1^{[-1]} = (\tilde{E}^1 + z_3 \tilde{E}^4) l_1 \\ q_2^{[1]} \equiv w_2^{[1]} - w_2^{[-1]} = \frac{1}{2} (\tilde{E}^3 + z_3 \tilde{E}^6) l_1 \\ q_3^{[1]} \equiv w_3^{[1]} - w_3^{[-1]} = (\tilde{E}^8 - \frac{z_3}{2} \tilde{E}^6) l_1 \end{array} \right. \quad \text{and} \quad \left\{ \begin{array}{l} q_1^{[2]} \equiv w_1^{[2]} - w_1^{[-2]} = \frac{1}{2} (\tilde{E}^3 + z_3 \tilde{E}^6) l_2 \\ q_2^{[2]} \equiv w_2^{[2]} - w_2^{[-2]} = (\tilde{E}^2 + z_3 \tilde{E}^5) l_2 \\ q_3^{[2]} \equiv w_3^{[2]} - w_3^{[-2]} = (\tilde{E}^7 - \frac{z_3}{2} \tilde{E}^6) l_2 \end{array} \right. \quad (\text{A2})$$

where subscripts $[\pm i]$ indicate values on boundary surfaces $\partial Y_{[\pm i]}$; see Figure 4. Thus, the original governing Equation (6) to be solved for \mathbf{u}^* is replaced by the following, to be solved for \mathbf{w} :

$$\left\{ \begin{array}{l} \partial_y^T \boldsymbol{\sigma} = 0 \\ \boldsymbol{\sigma} = \mathbf{C} (\boldsymbol{\varepsilon} - \boldsymbol{\varepsilon}^{\text{th}}) \\ \boldsymbol{\varepsilon} = \partial_y \mathbf{w} \\ \text{with (A2)} \end{array} \right. \quad (\text{A3})$$

Here, all the components of the generalized macroscopic strain $\tilde{\mathbf{E}}$ are given as data in the constraint conditions (A2).

To evaluate the plate stiffness matrix, given eight patterns of unit generalized macroscopic strain vectors, we conduct eight sets of NPTs by solving (A3) with $\Delta T = 0$. For example, when the unit strain vector representing Mode 1 deformation is

$$\{ \tilde{E}^1 \ \tilde{E}^2 \ \tilde{E}^3 \ \tilde{E}^4 \ \tilde{E}^5 \ \tilde{E}^6 \ \tilde{E}^7 \ \tilde{E}^8 \} = \{ \hat{E}^1 \ 0 \ 0 \ 0 \ 0 \ 0 \ 0 \ 0 \}$$

where $\hat{E}^1 = 1$, the constraint conditions yield

$$y_1 - \text{surface} : \left\{ \begin{array}{l} w_1^{[1]} - w_1^{[-1]} = \hat{E}^1 l_1 \\ w_2^{[1]} - w_2^{[-1]} = 0 \\ w_3^{[1]} - w_3^{[-1]} = 0 \end{array} \right. , \quad y_2 - \text{surface} : \left\{ \begin{array}{l} w_1^{[2]} - w_1^{[-2]} = 0 \\ w_2^{[2]} - w_2^{[-2]} = 0 \\ w_3^{[2]} - w_3^{[-2]} = 0 \end{array} \right. \quad (\text{A5})$$

Then, by solving the microscopic problem governed by Equation (A3) with these settings, we compute the generalized macroscopic stress $\tilde{\mathbf{M}}^{\text{out}}$ using Equations (7) and (8), which can be identified with the first column vector of $\tilde{\mathbf{D}}$ in Equation (9); that is, $\tilde{D}_{i1} = \tilde{M}_i^{\text{out}}$.

Also, by preparing the input datum as

$$\{ \tilde{E}^1 \ \tilde{E}^2 \ \tilde{E}^3 \ \tilde{E}^4 \ \tilde{E}^5 \ \tilde{E}^6 \ \tilde{E}^7 \ \tilde{E}^8 \} = \{ 0 \ 0 \ 0 \ 0 \ 0 \ 0 \ 0 \ 0 \} \quad \text{and} \quad \Delta T = 1 \quad (\text{A6})$$

we solve (A3) to evaluate the generalized macroscopic stress $\tilde{\mathbf{M}}^{\text{out}}$, which corresponds to the generalized macroscopic thermal stress, because $\tilde{M}_i^{\text{th}} = -\tilde{M}_i^{\text{out}}$.

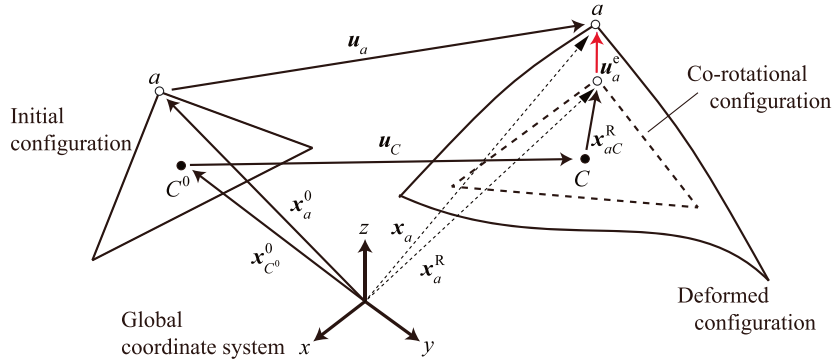
It must be noted that the microscopic problem (A3) is indefinite when conducting NPTs for Modes 7 and 8. In fact, when an in-plane unit cell is subjected to macroscopic transverse shear deformations, its rigid body rotations are activated. To suppress the rigid body motion of the in-plane unit cell, the following additional constraint conditions must be imposed:

$$\int_{-h/2}^{h/2} \int_{-l_1/2}^{l_1/2} \int_{-l_2/2}^{l_2/2} w_2 y_3 dy_1 dy_2 dy_3 = 0 \quad \text{and} \quad \int_{-h/2}^{h/2} \int_{-l_1/2}^{l_1/2} \int_{-l_2/2}^{l_2/2} w_1 y_3 dy_1 dy_2 dy_3 = 0 \quad (\text{A7})$$

For more details, refer to Reference [25].

APPENDIX B: CO-ROTATIONAL FORMULATION

This appendix presents supplemental explanations for the co-rotational (CR) formulation [31]. The definitions of the local coordinate systems and the related coordinate transformation rules are particularly important in this formulation, but the way these are defined depends on the shape or type of FE used [43]. In this appendix, we only consider the three-node triangular flat shell element [44, 45] that we use exclusively in the proposed two-scale structural topology optimization method.

Figure B.1. Schematic of elastic displacement u^e .

First, the origin C^0 of the initial coordinate system is selected at the centroid of each FE so that its position vector can be defined as

$$\mathbf{x}_{C^0}^0 = \frac{1}{3} \sum_{a=1}^3 \mathbf{x}_a^0 \quad (\text{B1})$$

where \mathbf{x}_a^0 is the position vectors of nodes a ($a = 1, 2, 3$) constituting the element; see Figure 5. Next, the first basis vector \mathbf{e}_1^0 is set parallel to the edge of the element connecting nodes 1 and 2, as $\mathbf{e}_1^0 = \mathbf{x}_{21}^0 / \|\mathbf{x}_{21}^0\|$, where \mathbf{x}_{21}^0 is the direction vector $\mathbf{x}_{21}^0 = \mathbf{x}_2^0 - \mathbf{x}_1^0$, and the third base vector \mathbf{e}_3^0 is set normal to the plane of the element as $\mathbf{e}_3^0 = \mathbf{x}_{21}^0 \times \mathbf{x}_{31}^0 / \|\mathbf{x}_{21}^0 \times \mathbf{x}_{31}^0\|$. Then, the second basis \mathbf{e}_2^0 is determined to yield the Cartesian coordinates as $\mathbf{e}_2^0 = \mathbf{e}_3^0 \times \mathbf{e}_1^0$. Finally, the coordinate transformation matrix \mathbf{T}_0 from the global to initial coordinate systems is obtained as

$$\mathbf{T}_0 = [\mathbf{e}_1^0 \quad \mathbf{e}_2^0 \quad \mathbf{e}_3^0]^T \quad (\text{B2})$$

The coordinate transformation matrix \mathbf{T} operating from the global to CR coordinate systems can also be defined in a similar manner.

Referring to the schematic in Figure B.1, we define the displacement vector caused by elastic deformation only (hereafter called ‘elastic displacement’) in the global coordinate system. Let \mathbf{x}_a and \mathbf{x}_a^R be the total motions and the motions of nodes a ($a = 1, 2, 3$), respectively, the latter of which is caused by the elastic displacement only. The elastic displacement vector \mathbf{u}_a^e can now be defined as

$$\mathbf{u}_a^e = \mathbf{x}_a - \mathbf{x}_a^R = (\mathbf{u}_a + \mathbf{x}_a^0) - (\mathbf{x}_{C^0}^0 + \mathbf{u}_C + \mathbf{x}_{aC}^R) \quad (\text{B3})$$

because $\mathbf{x}_a = \mathbf{u}_a + \mathbf{x}_a^0$ and $\mathbf{x}_{aC}^R = \mathbf{x}_a^R - \mathbf{x}_C$, with $\mathbf{x}_C = \mathbf{x}_{C^0}^0 + \mathbf{u}_C$. Here, \mathbf{u}_a is the total displacement vectors of nodes a , \mathbf{u}_C is the total displacement vector of the centroid C , and \mathbf{x}_C is the motion of the centroid of deformed element C . The elastic displacement $\bar{\mathbf{u}}_a^e$ in the CR coordinate system is then obtained as

$$\bar{\mathbf{u}}_a^e = \mathbf{T} \mathbf{u}_a^e = \mathbf{T} (\mathbf{u}_a + \mathbf{x}_a^0 - \mathbf{x}_{C^0}^0 - \mathbf{u}_C) - \bar{\mathbf{x}}_{aC^0}^0 \quad (\text{B4})$$

given that $\bar{\mathbf{x}}_{aC^0}^0 = \bar{\mathbf{x}}_{aC^0}^R = \mathbf{T} \mathbf{x}_{aC^0}^R$.

Next, we define rotation matrices for the element configurations. The total rotation matrices \mathbf{R}_a for nodes a in the global coordinate system are related to the rotation matrices \mathbf{R}_a^e caused by the elastic displacement (hereafter called the ‘elastic rotation matrices’) in the CR coordinate system, with

$$\mathbf{R}_a^e = \mathbf{R}_a \mathbf{R}^{0T} \quad (\text{B5})$$

where \mathbf{R}^0 is the rotation matrix depending on the rigid body motion only, so it can be interpreted as a transformation matrix from the initial coordinate system to the CR coordinate system, such that

$$\mathbf{R}^0 = \mathbf{T}^T \mathbf{T}^0 \quad (\text{B6})$$

This implies that the total rotation matrices \mathbf{R}_a for nodes a can be decomposed into the elastic rotation and rigid body motion components by multiplication; see Reference [31] for more details. As a result, the elastic rotation matrices for nodes a in the CR coordinate system are obtained as

$$\overline{\mathbf{R}}_a^e = \mathbf{T}\mathbf{R}_a^e\mathbf{T}^T = \mathbf{T}\mathbf{R}_a\mathbf{T}^{0T} \quad (\text{B7})$$

based on Equations (B5) and (B6).

To define the coordinate transformation from the global to CR coordinate systems, we here define the following pseudo-vector that accommodates the degrees-of-freedom (DOFs) of the rotation:

$$\boldsymbol{\theta} = \frac{\theta}{2 \sin \theta} \{R_{(3,2)} - R_{(2,3)} \quad R_{(1,3)} - R_{(3,1)} \quad R_{(2,1)} - R_{(1,2)}\} \quad (\text{B8})$$

$$\theta = \|\boldsymbol{\theta}\| \quad (\text{B9})$$

where $R_{(i,j)}$ indicates the (i,j) -components of \mathbf{R} . The pseudo-vector $\overline{\boldsymbol{\theta}}_a^e$ for the elastic rotation matrix $\overline{\mathbf{R}}_a^e$ can also be defined in a similar fashion. We note that the elastic rotation pseudo-vector cannot be updated additively in 3D finite rotation problem [31]. We therefore introduce the following 3D infinitesimal incremental rotation vector, $\delta\boldsymbol{\omega}_a^e$:

$$\mathbf{R}_{a,\text{new}} = \mathbf{R}(\delta\boldsymbol{\omega}_a^e)\mathbf{R}_{a,\text{old}} \quad (\text{B10})$$

where

$$\mathbf{R}(\delta\boldsymbol{\omega}_a^e) = \mathbf{I} + \frac{\sin(\delta\omega_a^e)}{\delta\omega_a^e} \text{spin}(\delta\boldsymbol{\omega}_a^e) + \frac{1}{2} \left[\frac{\sin(\delta\omega_a^e/2)}{\delta\omega_a^e} \text{spin}(\delta\boldsymbol{\omega}_a^e)^2 \right] \quad \text{and} \quad \delta\omega_a^e = \|\delta\boldsymbol{\omega}_a^e\| \quad (\text{B11})$$

Here, $\delta\overline{\boldsymbol{\omega}}_a^e$ is related to the incremental rotational pseudo-vector $\delta\overline{\boldsymbol{\theta}}$ as in [31]

$$\delta\overline{\boldsymbol{\theta}}_a^e = \overline{\mathbf{H}}_a(\overline{\boldsymbol{\theta}}_a^e)\delta\overline{\boldsymbol{\omega}}_a^e \quad (\text{B12})$$

$$\overline{\mathbf{H}}_a(\overline{\boldsymbol{\theta}}_a^e) = \mathbf{I} - \frac{1}{2} \text{spin}(\overline{\boldsymbol{\theta}}_a^e) + \eta \text{spin}(\overline{\boldsymbol{\theta}}_a^e)^2 \quad (\text{B13})$$

where η is calculated as

$$\eta = \frac{1 - \frac{1}{2}\overline{\theta}_a^e \cot \frac{1}{2}\overline{\theta}_a^e}{\overline{\theta}_a^{e2}} \simeq \frac{1}{12} + \frac{1}{720}\overline{\theta}_a^{e2} \quad (\text{B14})$$

$$\overline{\boldsymbol{\theta}}_a^e = \|\overline{\boldsymbol{\theta}}_a^e\| \quad (\text{B15})$$

Also, $\text{spin}(\mathbf{a})$ is the operation to transform vector $\mathbf{a} = \{a_1, a_2, a_3\}$ to an equivalent matrix such that

$$\text{spin}(\mathbf{a}) = \begin{bmatrix} 0 & -a_3 & a_2 \\ a_3 & 0 & -a_1 \\ -a_2 & a_1 & 0 \end{bmatrix} \quad (\text{B16})$$

Accordingly, respectively denoting the generalized incremental elastic displacement vector in the CR coordinate system and the generalized incremental total displacement vector in the global coordinate system as $\delta\overline{\mathbf{p}}^e = \{\delta\overline{\mathbf{u}}^e, \delta\overline{\boldsymbol{\omega}}^e\}$ and $\delta\mathbf{d} = \{\delta\mathbf{u}, \delta\boldsymbol{\theta}\}$, respectively, we identify their relationship as follows:

$$\delta\overline{\mathbf{p}}_a^e = \boldsymbol{\Lambda}\delta\mathbf{d} \quad (\text{B17})$$

The specific components of this matrix $\boldsymbol{\Lambda}$ are too lengthy to express here, but reproduced in Reference [31].

ACKNOWLEDGMENTS

This work was supported by CSTI and NEDO, SIP (Innovative design/manufacturing technologies).

REFERENCES

1. Bendsøe MP, Kikuchi N. Generating optimal topologies in structural design using a homogenization method. *Computer Methods in Applied Mechanics and Engineering* 1988; **71**:197–224.
2. Suzuki K, Kikuchi N. A homogenization method for shape and topology optimization. *Computer Methods in Applied Mechanics and Engineering* 1991; **93**:291–318.
3. Eschenauer HA, Olhoff N. Topology optimization of continuum structures: a review. *Applied Mechanics Reviews* 2001; **54**(4):331–390.
4. Bendsoe MP, Sigmund O. *Topology Optimization. Theory, Methods, and Applications*. Springer: Berlin, 2004.
5. Rozvany GIN. A critical review of established methods of structural topology optimization. *Structural and Multidisciplinary Optimization* 2009; **37**(3):217–237.
6. Sigmund O, Maute K. Topology optimization approaches. A comparative review. *Structural and Multidisciplinary Optimization* 2013; **48**(6):1031–1055.
7. Terada K, Kikuchi N. A class of general algorithms for nonlinear multi-scale analyses of heterogeneous media. *Computer Methods in Applied Mechanics and Engineering* 2001; **190**:5427–5464.
8. Rodrigues H, Guedes JM, Bendsoe MP. Hierarchical optimization of material and structure. *Structural and Multidisciplinary Optimization* 2002; **24**:1–10.
9. Nakshatrala PB, Tortorelli DA, Nakshatrala KB. Nonlinear structural design using multi scale topology optimization. Part I. *Computer Methods in Applied Mechanics and Engineering* 2013; **261–262**:167–176.
10. Sivapuram R, Dunning PD, Kim HA. Simultaneous material and structural optimization by multiscale topology optimization. *Structural and Multidisciplinary Optimization* 2016; **54**(5):1267–1281.
11. Huang X, Zhou SW, Xie YM, Li Q. Topology optimization of microstructures of cellular materials and composites for macrostructure. *Computational Materials Science* 2013; **67**:397–407.
12. Kato J, Yachi D, Terada K, Kyoya T. Topology optimization of micro-structure for composites applying a decoupling multi-scale analysis. *Structural and Multidisciplinary Optimization* 2014; **49**:595–608.
13. Terada K, Kato J, Hirayama N, Inugai T, Yamamoto K. A method of two-scale analysis with micro-macro decoupling scheme: application to hyperelastic composite materials. *Computational Mechanics* 2013; **52**:1199–1219.
14. Vicente WM, Zuo ZH, Calixto TKL, Picelli R, Xie YM. Concurrent topology optimization for minimizing frequency responses of two-level hierarchical structures. *Computer Methods in Applied Mechanics and Engineering* 2016; **301**:116–136.
15. Yan X, Huang X, Zha Y, Xie YM. Concurrent topology optimization of structures and their composite microstructures. *Computers & Structures* 2014; **133**:103–110.
16. Xia L, Breitkopf P. Concurrent topology optimization design of material and structure within FE² nonlinear multiscale analysis framework. *Computer Methods in Applied Mechanics and Engineering* 2014; **278**:1524–542.
17. Xia L, Breitkopf P. Multiscale structural topology optimization with an approximate constitutive model for local material microstructure. *Computer Methods in Applied Mechanics and Engineering* 2015; **286**:1147–167.
18. Long K, Han D, Gu X. Concurrent topology optimization of composite macrostructure and microstructure constructed by constituent phases of distinct Poisson's ratios for maximum frequency. *Computational Materials Science* 2017; **129**:194–201.
19. Da DC, Cui XY, Long K, LI GY. Concurrent topological design of composite structures and the underlying multi-phase materials. *Computers and Structures* 2017; **179**:1–14.
20. Sanchez-Palencia E. *Non-homogeneous Media and Vibration Theory*, Lecture Notes in Physics, vol. 127. Springer-Verlag: Berlin, 1980.
21. Suquet PM. Elements of homogenization theory for inelastic solid mechanics. In *Homogenization Techniques for Composite Media*, Sanchez-Palencia E, Zaoui A (eds). Springer-Verlag: Berlin; 193–278, 1987.
22. El-Sabbagh A, Wael A, Baz A. Topology optimization of periodic Mindlin plates. *Finite Element in Analysis and Design* 2008; **44**:439–449.
23. Rathbun HJ, Zok FW, Evans AG. Stren optimization of metallic sandwich panels subject to bending. *International Journal of Solids and Structures* 2005; **42**:6643–6661.
24. Liu T, Deng ZC, Lu TJ. Design optimization of truss-cored sandwiches with homogenization. *International Journal of Solids and Structures* 2006; **43**:7891–7918.
25. Terada K, Hirayama N, Yamamoto K, Muramatsu M, Matsubara S, Nishi S. Numerical plate testing for linear two scale analyses of composite plates with in-plane periodicity. *International Journal for Numerical Methods in Engineering* 2016; **105**:111–137.
26. Buhl T, Pedersen CBW, Sigmund O. Stiffness design of geometrically nonlinear structures using topology optimization. *Structural and Multidisciplinary Optimization* 2000; **19**:93–104.
27. Bruns TE, Tortorelli DA. Topology optimization of non-linear elastic structures and compliant mechanisms. *Computer Methods in Applied Mechanics and Engineering* 2001; **16**:3443–3459.
28. Gea HC, Luo J. Topology optimization of structures with geometrical nonlinearities. *Computers and Structures* 2001; **79**:1977–1985.

29. Hung D, Gea HC. Topology optimization of nonlinear structures. *Finite Elements in Analysis and Design* 2004; **40**:1417–1427.
30. Cho S, Jung HS. Design sensitivity analysis and topology optimization of displacement-loaded non-linear structures. *Computer Methods in Applied Mechanics and Engineering* 2003; **192**:2539–2553.
31. Felippa CA, Haugen B. A unified formulation of small-strain corotational finite elements: I. Theory. *Computer Methods in Applied Mechanics and Engineering* 2005; **194**:2285–2335.
32. Almeida FS, Awruch AM. Corotational nonlinear dynamic analysis of laminated composite shells. *Finite Elements in Analysis and Design* 2011; **47**:1131–1145.
33. Yang JS, Xia PJ. Finite element corotational formulation for geometric nonlinear analysis of thin shells with large rotation and small strain. *Science China Technological Sciences* 2012; **55**(11):3124–3152.
34. Gao T, Zhang W. Topology optimization involving thermo-elastic stress loads. *Structural and Multidisciplinary Optimization* 2010; **42**:725–738.
35. Stolpe M, Svanberg K. An alternative interpolation scheme for minimum compliance topology optimization. *Structural and Multidisciplinary Optimization* 2001; **22**:116–124.
36. Patnaik SN, Gupta JD, Berke L. Murtis and limitations of optimality criteria method for structural optimization. *International Journal for Numerical Methods in Engineering* 1995; **38**:3087–3120.
37. Svanberg K. A class of globally convergent optimization method based on conservative convex separable approximation. *SIAM Journal on Optimization* 2002; **12**(2):555–573.
38. Borrvall T. Topology optimization of elastic continua using restriction. *Archives of Computational Methods in Engineering* 2001; **8**(4):351–385.
39. Wang MY, Wang S. Bilateral filtering for structural topology optimization. *International Journal for Numerical Methods in Engineering* 2005; **63**:1911–1938.
40. Sigmund O. Morphology-based black and white filters for topology optimization. *Structural and Multidisciplinary Optimization* 2007; **33**:401–424.
41. Bourdin B. Filters in topology optimization. *International Journal for Numerical Methods in Engineering* 2001; **50**(9):2143–2158.
42. Svanberg K, Svärd H. Density filters for topology optimization based on the Pythagorean means. *Structural and Multidisciplinary Optimization* 2013; **48**:859–875.
43. Battini JM, Pacoste C. On the choice of the linear element for corotational triangular shells. *Communications In Numerical Methods In Engineering* 2006; **195**:6362–6377.
44. Bergan PG, Felippa CA. A triangular membrane element with rotational degrees of freedom. *Computer Methods in Applied Mechanics and Engineering* 1985; **50**:25–69.
45. Felippa CA. A study of optimal membranetTriangles with drilling freedoms. In *Center for Aerospace Structures*, Report CU-CAS-03-02, 2003.